Large-Eddy Simulations of Marine Boundary Layer Clouds Associated with Cold-Air Outbreaks during the ACTIVATE Campaign. Part II: Aerosol–Meteorology–Cloud Interaction

Xiang-Yu Li,[a] Hailong Wang,[a] Jingyi Chen,[a] Satoshi Endo,[b] Simon Kirschler,[c,d] Christiane Voigt,[c,d] Ewan Crosbie,[e,f] Luke D. Ziemba,[e] David Painemal,[e,f] Brian Cairns,[g] Johnathan W. Hair,[e] Andrea F. Corral,[h] Claire Robinson,[f] Hossein Dadashazar,[h] Armin Sorooshian,[h,i] Gao Chen,[e] Richard Anthony Ferrare,[e] Mary M. Kleb,[e] Hongyu Liu,[j] Richard Moore,[e] Amy Jo Scarino,[f,e] Michael A. Shook,[e] Taylor J. Shingler,[e] Kenneth Lee Thornhill,[f,e] Florian Tornow,[g,k] Heng Xiao,[a] and Xubin Zeng[i]

[a] *Pacific Northwest National Laboratory, Richland, Washington*
[b] *Brookhaven National Laboratory, Upton, New York*
[c] *Institut für Physik der Atmosphäre, Deutsches Zentrum für Luft- und Raumfahrt, Oberpfaffenhofen, Germany*
[d] *Institute for Physics of the Atmosphere, Johannes Gutenberg-University Mainz, Mainz, Germany*
[e] *NASA Langley Research Center, Hampton, Virginia*
[f] *Science Systems and Applications, Inc., Hampton, Virginia*
[g] *NASA Goddard Institute for Space Studies, New York, New York*
[h] *Department of Chemical and Environmental Engineering, The University of Arizona, Tucson, Arizona*
[i] *Department of Hydrology and Atmospheric Sciences, The University of Arizona, Tucson, Arizona*
[j] *National Institute of Aerospace, Hampton, Virginia*
[k] *Center for Climate Systems Research, Earth Institute, Columbia University, New York, New York*

ABSTRACT: Aerosol effects on micro/macrophysical properties of marine stratocumulus clouds over the western North Atlantic Ocean (WNAO) are investigated using in situ measurements and large-eddy simulations (LES) for two cold-air outbreak (CAO) cases (28 February and 1 March 2020) during the Aerosol Cloud Meteorology Interactions over the Western Atlantic Experiment (ACTIVATE). The LES is able to reproduce the vertical profiles of liquid water content (LWC), effective radius r_{eff} and cloud droplet number concentration N_c from fast cloud droplet probe (FCDP) in situ measurements for both cases. Furthermore, we show that aerosols affect cloud properties (N_c, r_{eff}, and LWC) via the prescribed bulk hygroscopicity of aerosols ($\overline{\kappa}$) and aerosol size distribution characteristics. N_c, r_{eff}, and liquid water path (LWP) are positively correlated to $\overline{\kappa}$ and aerosol number concentration (N_a) while cloud fractional cover (CFC) is insensitive to $\overline{\kappa}$ and aerosol size distributions for the two cases. The realistic changes to aerosol size distribution (number concentration, width, and the geometrical diameter) with the same meteorology state allow us to investigate aerosol effects on cloud properties without meteorological feedback. We also use the LES results to evaluate cloud properties from two reanalysis products, ERA5 and MERRA-2. Compared to LES, the ERA5 is able to capture the time evolution of LWP and total cloud coverage within the study domain during both CAO cases while MERRA-2 underestimates them.

KEYWORDS: Cloud forcing; Cloud microphysics; Cloud radiative effects

1. Introduction

Aerosols and clouds pose the largest uncertainty in climate projection since they mediate the radiative forcing of Earth's atmosphere (Seinfeld et al. 2016). An increased loading of aerosols in the atmosphere reflects more incoming solar energy to space and consequently cools the Earth system. The increased aerosol number concentration N_a in an environment with constant liquid water content (LWC) leads to cloud droplets with smaller size and larger number concentration N_c, which makes the cloud more reflective, often called the first indirect effect, aka the Twomey effect (Twomey 1977). Reduced droplet sizes can also result in less precipitation and longer cloud lifetime. The latter effect is known as the second indirect effect (Albrecht 1989). Cloud radiative properties are determined by both the cloud macrophysical properties, such as the liquid water path (LWP) and cloud fractional coverage (CFC), and by the cloud microphysical properties, such as N_c and the effective radius r_{eff}. Global mean change in radiative forcing due to anthropogenic aerosols, relative to preindustrial era (before year 1850), is roughly estimated to be between -1.6 and -0.6 W m^{-2} with a 68% confidence interval in the years 2005–15 (Bellouin et al. 2020). However, how the

anthropogenic aerosols affect LWC and CFC remains unclear (Bellouin et al. 2020; McCoy et al. 2020), which is due to the fact that LWC and CFC are predominantly determined by meteorology states but also modulated by changes in N_c through precipitation (Stevens and Feingold 2009). This is the aerosol–meteorology–cloud-interaction (AMCI) problem that encompasses a wide range of spatial–temporal scales from nm-sized aerosol particles to large-scale atmospheric circulations [$\mathcal{O}(100)$ km]. Global Earth system models and even cloud-resolving models suffer from coarse resolutions such that vital cloud macro/microprocesses in the marine boundary layer cannot be physically represented.

Here, we focus on AMCI processes in marine boundary layer stratocumulus, which is a canonical cloud regime for studying AMCI as this regime is often in an emergent state of precipitation and is sensitive to AMCI (Feingold et al. 2010; Seifert et al. 2015). In this case, an increased N_c may lead to either increased LWC due to the suppression of precipitation (Albrecht 1989) or reduced LWC due to enhanced entrainment of dry air (Ackerman et al. 2004; Chen et al. 2011). The overall effects of increasing N_c on LWC depend on the meteorology states in different cloud regimes. For example, Sandu et al. (2008) shows that LWP reduction of the polluted clouds is amplified by decoupling of the boundary layer during the day. The suppression of precipitation may alter CFC by either increasing the cloud lifetime (Albrecht 1989) or by influencing the transitioning from open to closed Rayleigh–Bénard cells of stratocumulus (Rosenfeld et al. 2006; Wang and Feingold 2009a), or by altering mesoscale circulation and lower-level moisture convergence (Wang and Feingold 2009b). Nevertheless, the response of LWP and CFC to N_c is still uncertain based on observational and general circulation model (GCM) studies. GCMs typically show a positive correlation between LWP and N_c and between CFC and N_c due to a direct reduction in the autoconversion of cloud droplets to raindrops by increased N_c, which is parameterized for the collision–coalescence process (Ghan et al. 2016; Bellouin et al. 2020). Using large-eddy simulations (LES) with prescribed constant N_c, Seifert et al. (2015) showed that the suppression of precipitation due to increased N_c reduces CFC in trade wind cumulus. However, this effect is compensated for by the Twomey effect as the overall effect of aerosols on cloud albedo is small. LES with more complete and resolved physical processes, informed and validated by observations, is needed to unravel discrepancies in GCMs regarding AMCI.

AMCI associated with marine cold-air outbreaks (CAO) is poorly understood and has been rarely studied due to more complicated CAO cloud processes and a lack of measurements. De Roode et al. (2019) performed an LES intercomparison of a CAO case to quantify the turbulent transport at length scales between 1 and 10 km and to study the sensitivity of the CAO to N_c and ice microphysics. Using the same microphysics scheme (Seifert and Beheng 2006) and prescribed constant N_c, the Dutch Atmospheric LES, the Max-Planck Institute for Meteorology (MPI) LES, and the Parallelized Large Eddy Simulation Model for Atmospheric and Oceanic Flows (PALM) obtained very different CFC, LWP, and

surface precipitation in both magnitude and timing. They also showed that a reduction of N_c results in a stronger precipitation, smaller LWP and earlier breakup of clouds, which is consistent with the findings for subtropical marine stratocumulus in Wang and Feingold (2009a). As marine CAOs are generally associated with mixed-phase clouds (Fletcher et al. 2016), proper characterization and simulation of ice microphysics are expected to be critical for AMCI (Hu et al. 2023). Substantial spread among LES models in ice water content (IWC) due to different parameterizations of ice microphysics was observed in de Roode et al. (2019). Tornow et al. (2021) examined the role of the riming process in marine CAO using LES with a prescribed single-mode lognormal aerosol-size distributions and two-moment Morrison cloud microphysics scheme. They showed that increasing a diagnostic ice nuclei particle concentration intensifies early and light precipitation, which accelerates the stratocumulus breakup. In addition, Tornow et al. (2021) showed that only a prognostic aerosol treatment produced plausible cloud regime transitions and indicated that a prognostic INP concentration is needed to capture ice multiplication near the cloud breakup that has often been observed. However, these LES studies did not explore how N_c impacted by a realistic setup of several aerosol modes and their hygroscopicity modulates LWP, CFC, and radiation fluxes during CAO. Therefore, a prognostic N_c, based on model resolved meteorology and measured aerosol size distributions and hygroscopicity, is important in understanding AMCI.

The western North Atlantic Ocean (WNAO) region is characterized by a complicated climate system that features weather processes involving a wide range of spatial–temporal scales (Sorooshian et al. 2020). The sea surface temperature (SST) in the WNAO exhibits sharp spatial gradients due to the Gulf stream, which, together with strong wind, lead to strong surface heat fluxes within the atmospheric boundary layer (Painemal et al. 2021b). This creates ideal conditions for CAO events as investigated in Seethala et al. (2021) and Li et al. (2022, hereafter Part I). Aerosols transported from sources over the continental United States, generated over ocean from shipping emissions and sea spray, and produced by long-range transport of smoke and dust (Corral et al. 2021; Aldhaif et al. 2020, 2021) contribute to the total aerosol number concentration in WNAO. AMCI is poorly understood in this region, which is partly due to limited in situ measurements of aerosol and cloud microphysical processes (Sorooshian et al. 2019). The Aerosol Cloud Meteorology Interactions over the Western Atlantic Experiment (ACTIVATE) campaign aims to unravel AMCI in WNAO by collecting unprecedented in situ and remote sensing statistics of aerosols and cloud properties. To achieve this, the dual-aircraft approach is being adopted for about 150 flights (~600 joint total flight hours) during 2020–22 in the WNAO region (25°–50°N, 60°–85°W). The lower-flying HU-25 Falcon (a minimum altitude of 150 m) focuses on measuring in situ trace gases, aerosol, cloud properties, thermodynamics, and precipitation. The higher-flying King Air (nominal flight altitude of 9 km) simultaneously acquires remote sensing retrievals of aerosols and
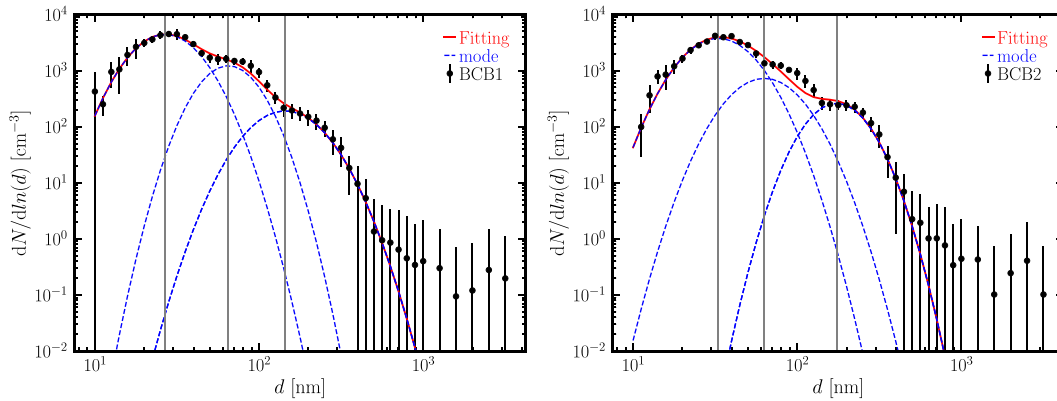
FIG. 1. Aerosol size distributions (black dots) obtained from SMPS and LAS measurements for the 28 Feb case during the BCB legs with the error bars indicating $\pm\sigma$. The dashed blue curves represent lognormal fitting of individual modes and the red curve is for the final fitted size distribution. Fitting parameters are listed in Table 1. Only particles within 10 nm–1 μm are used for the fitting.

clouds and deploys dropsondes to measure the meteorological states (Sorooshian et al. 2019).

We aim to study AMCI in the WNAO region by performing LES, constrained and evaluated by the ACTIVATE measurements. The measured aerosol size distributions and hygroscopicity, which provide a more realistic cloud condensation nuclei (CCN) pool, are fed into a two-moment microphysics scheme in the LES, compared to a fixed CCN for the prognostic N_c used in previous LES studies. To our knowledge, the investigation of AMCI in a fast-evolving marine boundary layer associated with CAO over the WNAO region using process-oriented model simulations constrained with in situ measurements of aerosols, clouds, and meteorological conditions has never been done. The limited-domain process simulations use large-scale forcings from reanalysis products, which are also evaluated against ACTIVATE observational data. Furthermore, ameliorated understanding of AMCI and quantification of aerosol–cloud relationships from LES can serve as a benchmark to evaluate and improve parameterizations of aerosol–cloud processes in global and regional models. We also demonstrate this by comparing cloud properties between the LES and reanalysis products for the two cases studied here.

Using the same large-scale forcing strategy as in Endo et al. (2015), Part I investigated the marine boundary layer (BL) and clouds during two CAO events (28 February and 1 March 2020), which are characterized by strong temporally and spatially varying meteorological states in the WNAO region. It focused on the sensitivities of WRF-LES to large-scale forcing and surface heat fluxes validated by the ACTIVATE measurements. In this companion study of Part I, we focus on aerosol effects on clouds under the two CAO conditions. As mentioned above, we use WRF-LES with prognostic N_c based on measured aerosol properties, compare model results with the ACTIVATE cloud measurements, and evaluate cloud macrophysical properties in reanalysis products for the two CAO events reported in Part I. The reminder of the paper is organized as follows. In section 2, we describe ACTIVATE

measurements, reanalysis data, and satellite retrievals used in this study. Section 3 summarizes the WRF-LES numerical experiment setup. Section 4 discusses WRF-LES simulated aerosol effects on CAO clouds in two cases with comparison to ACTIVATE measurements. Section 5 compares the LES BL structure and clouds with reanalysis and satellite retrievals. We conclude in section 6.

2. Observations, reanalysis, and satellite retrievals

a. Aerosol size distribution

Aerosol particles with diameter d between 3 and 100 nm were measured by the Scanning Mobility Particle Sizer (SMPS; TSI model 3085 differential mobility analyzer and TSI model 3776 condensation particle counter) and those with sizes larger than 100 nm were measured by the Laser Aerosol Spectrometer (LAS; TSI model 3340) equipped on the HU-25 Falcon. The uncertainty for both SMPS and LAS measurements is better than $\pm$10%–20% over the submicron aerosol size range (Moore et al. 2021). The sampling frequency is 1/60 and 1 Hz for SMPS and LAS, respectively.

The black dots in Fig. 1 represent the aerosol size distribution averaged over below cloud-base (BCB) flight legs, sampled by SMPS and LAS within the study domain (1600–1700 UTC) for the 28 February case. Two BCB flight legs were performed, marked as BCB1 and BCB2, as shown in Figs. A1a and A2a in appendix A. Only particles larger than 10 nm in diameter are shown, as smaller nucleation-mode particles are not likely contributing to the population of cloud condensation nuclei at realistic supersaturations. We fit the measured aerosol size distributions using a lognormal distribution function,

$$\frac{dN}{d\ln d} = \frac{N^*}{\sqrt{2\pi}\ln\sigma}\exp\left[-\frac{(\ln d - \ln\mu)^2}{2\ln^2\sigma}\right], \qquad (1)$$

where N^* is the total aerosol number concentration, and μ and σ are the geometric median diameter and the standard

TABLE 1. Fitted parameters of the aerosol size distribution for the 28 Feb case shown in Fig. 1.

BCB leg	Time (UTC)	N (cm^{-3})			μ (nm)			σ		
		N_1	N_2	N_3	μ_1	μ_2	μ_3	σ_1	σ_2	σ_3
BCB1	1546:53–1554:54	4222	994	198	26.7	64.9	144.5	1.46	1.38	1.51
BCB2	1643:41–1647:03	3757	723	219	33.0	63.0	173.7	1.49	1.49	1.40

deviation, respectively. The fitted parameters using three lognormal modes are listed in Table 1.

The aerosol size distribution for the 1 March case is shown in Fig. 2, and the corresponding fitted parameters and validation are listed in Table 2. Similar to the 28 February case, two BCB flight legs were performed as shown in Figs. A1b and A2b. Two and three lognormal modes are used for the fitting for BCB1 and BCB2, respectively. It is worth noting that the total aerosol number concentration of the largest mode from BCB2 is about 2.6 times larger than that from BCB1, suggestive of substantial spatiotemporal variation of aerosol particles below cloud base. Without interactive aerosol sources, we do not expect the LES to capture the spatial variation of size distribution and hygroscopicity of aerosols. Thus, a uniform size distribution and hygroscopicity is used within the simulation domain. The same aerosol treatment was used in Endo et al. (2015), who found that cloud macrophysical properties are insensitive, but cloud microphysical properties are sensitive, to aerosol hygroscopicity. However, they estimated the aerosol hygroscopicity according to Köhler theory using the aerosol size distribution and CCN concentration. We use direct measurements during the ACTIVATE campaign to ensure a more robust estimation of the bulk hygroscopicity of aerosols $\overline{\kappa}$ as discussed below.

b. Hygroscopicity of aerosol particles

The WRF-LES takes bulk hygroscopicity (κ) of each size mode, which can be estimated from κ and mass of each chemical component. The bulk κ of a solute aerosol particle with mixed component i is given by the simple volume mixing rule (Petters and Kreidenweis 2007)

$$\kappa = \sum_i \epsilon_i \kappa_i, \qquad (2)$$

where κ_i is the hygroscopicity parameter of each individual (dry) component of aerosol particles and is obtained from Table 1 of Petters and Kreidenweis (2007) for both the inorganic and organic components. The volume fraction ϵ_i of a component is given by

$$\epsilon_i = \frac{\dfrac{m_i}{\rho_i}}{\sum_i \dfrac{m_i}{\rho_i}}, \qquad (3)$$

where m_i is the mass concentration of each component and ρ_i is the material density of each component. The mass m_i of major components was measured by an Aerodyne High Resolution Time-of-Flight Aerosol Mass Spectrometer (HR-ToF-AMS) (DeCarlo et al. 2008). The uncertainty in measured mass concentrations is up to 50% due to uncertainties in the applied instrument collection efficiency, which was assumed to be unity for this dataset based on preliminary comparison with particle-into-liquid sampler (PILS) measurements. We take the time-averaged m_i for each BCB flight leg to calculate ϵ_i. The relative mass concentration of organics, sulfate (SO_4^{2-}), nitrate (NO_3^-), and ammonium (NH_4^+) from the AMS measurement are listed in Table A1 and the corresponding mass of $(NH_4)_2SO_4$ and NH_4NO_3 are listed in Table A2. A mass-weighted κ is calculated from AMS-measured organic, sulfate, and nitrate mass and by assuming both sulfate and nitrate are fully neutralized as $(NH_4)_2SO_4$ and NH_4NO_3 to assign appropriate κ values (Table A2). Ammonium concentrations measured by the AMS support this assumption. Time-averaged $\overline{\kappa}$ calculated according to Eq. (2) is listed in the last column of Table A1. We use same $\overline{\kappa}$ for different modes of aerosol size distributions even though Fridlind et al. (2017) indicates that smaller modes have smaller κ values.
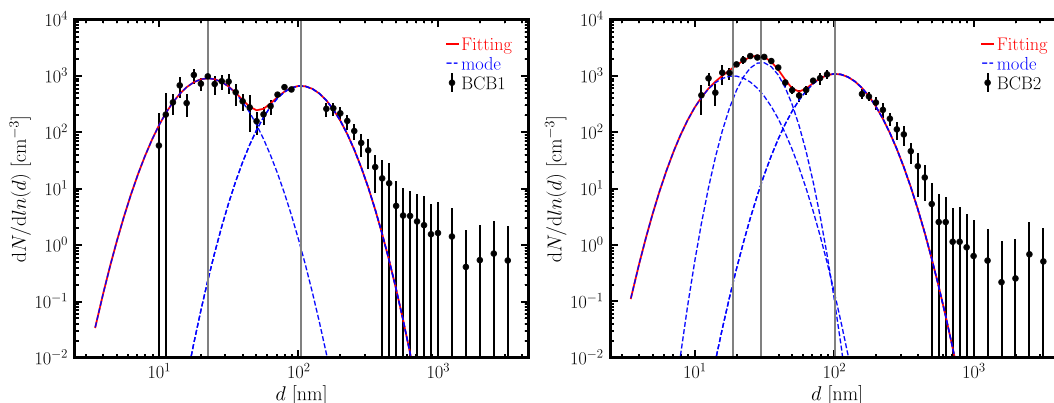

FIG. 2. As in Fig. 1, but for the 1 Mar case. Fitting parameters are listed in Table 2.

TABLE 2. Fitted parameters of the aerosol size distribution for the 1 Mar case shown in Fig. 2.

BCB leg	Time (UTC)	N (cm^{-3})			μ (nm)			σ		
		N_1	N_2	N_3	μ_1	μ_2	μ_3	σ_1	σ_2	σ_3
BCB1	1453:22–1501:45	940	645	—	22.4	104.2	—	1.51	1.47	—
BCB2	1551:21–1555:06	996	1192	1118	19.0	30.2	102.3	1.49	1.31	1.51

c. Droplet/ice size distribution

Cloud droplet/ice size distribution, liquid or ice water content (LWC or IWC), number concentration of cloud droplet (ice crystals) N_c (N_{ice}), and effective radius r_{eff} were measured by Fast Cloud Droplet Probe (FCDP) equipped on the HU-25 Falcon. The FCDP measures particles in a size range of 3–50 μm with an uncertainty of less than 20% (Baumgardner et al. 2017; Knop et al. 2021). The cutoff is 3.5 μm. The two-dimensional stereo (2DS) probe (Lawson et al. 2006) equipped on HU-25 measures size and concentration of cloud/ice particles in the range of 11.4–1464.9 μm in diameter with a spatial resolution of 11.4 μm pixel^{-1} (Voigt et al. 2010; Bansmer et al. 2018). However, the first size bin of 2DS measurement was excluded due to large uncertainties. Therefore, 2DS measurement covers a size range of 28.5–1464.9 μm in the present study.

d. ERA5 and MERRA-2

As described in Part I, large-scale forcings (i.e., moisture and temperature advective tendencies and wind profiles) and surface heat fluxes to drive the WRF-LES are obtained from hourly model-level and surface-level ERA5 data with a mesh grid-size of 31 km (Hersbach et al. 2020). The 3-hourly model-level and 1-hourly surface-level MERRA-2 (Gelaro et al. 2017) reanalysis data products with a horizontal resolution of 0.5° × 0.625° are used to compare with WRF-LES and ERA5.

e. GOES-16 satellite retrievals

We use retrievals from the Geostationary Operational Environmental Satellite (GOES) to evaluate ERA5/MERRA-2 and WRF-LES. GOES-16 Advanced Baseline Imager (ABI) retrievals (LWP, N_c, and r_{eff}) are produced using the Clouds and the Earth's Radiant Energy System (CERES) Edition 4 algorithms (Minnis et al. 2021; Trepte et al. 2019) adapted to geostationary satellites (Minnis et al. 2008). The GOES-16 products have a pixel size of 2 km and a selected time resolution of 20 min.

3. LES numerical experiment setup

The LES setup is the same as in Part I. The lateral size of the LES domain is $L_x = L_y = 60$ km with a grid spacing of $dx = dy = 300$ m. There are 153 vertical layers up to $z_{top} = 7$ km. Even though the horizontal model grid spacing of $dx = 300$ m is coarser than the commonly used $dx = 100$ m in LES modeling studies (Bryan et al. 2003; Lai et al. 2020), we have performed sensitivity tests for our CAO case studies and found that $dx = 300$ m is sufficient to resolve the important large eddies in the boundary layer and capture the observed cloud

properties, as shown in the comparison of turbulent fluxes and power spectra in Part I and kinetic energy in Fig. S1 in the online supplemental material, as well as in the comparison of LWP time series and vertical profiles of cloud and meteorological variables in Part I, by comparing to simulations at $dx = 100$ m and in situ turbulence measurements. It is worth noting that the choice of $dx = 300$ m is specifically for the strongly forced CAO cases being studied here in the idealized model configuration, which should not be generalized for other cases, especially for the purpose of resolving CAO cloud-roll structures. For instance, Lai et al. (2020) found that $dx = 111$ m can better capture the Arctic roll-cloud structures with wavelengths of 2–3 km than $dx = 333$ m does in the WRF nested-domain configuration. The periodic boundary condition is used in horizontal directions. All simulations start at 0600 UTC and end at 2100 UTC with a fixed time step of 3 s. The two-moment Morrison cloud microphysics scheme with prescribed aerosol size modes (see section 2a) and hygroscopicity (see section 2b) is employed (Endo et al. 2015). The same time-varying large-scale forcing (i.e., temperature and water vapor mixing ratio tendencies $\partial_t \overline{\theta}$ and $\partial_t \overline{q}_v$, wind speed u and v relaxation, and divergence $\overline{D}$) and surface heat fluxes described in Part I are adopted. To investigate the aerosol effects, we perform simulations with prescribed aerosol size distributions derived from the ACTIVATE campaign measurements as described in section 2a. Details of simulations are listed in Table 3.

4. Aerosol–meteorology–cloud interactions

The ultimate goal of this study is to investigate how aerosols affect cloud micro/macrophysical processes under different meteorological conditions of two CAO cases. The 28 February

TABLE 3. List of simulations. "NC" denotes prescribed cloud droplet number concentration, and "NA" denotes prescribed aerosol number concentration. BCB flight legs and $\overline{\kappa}$ are consistent with the values listed in Table A2. The mean κ of each aerosol component ($\overline{\kappa}$) is used in the simulations unless otherwise specified. 0228_NA1_$\overline{\kappa}_{org}$ and 0228_NA1_κ_{org}^{max} denote simulations with $\overline{\kappa}_{org}$ and κ_{org}^{max}, respectively. Simulations 0228_NC and 0301_NC are from Part I.

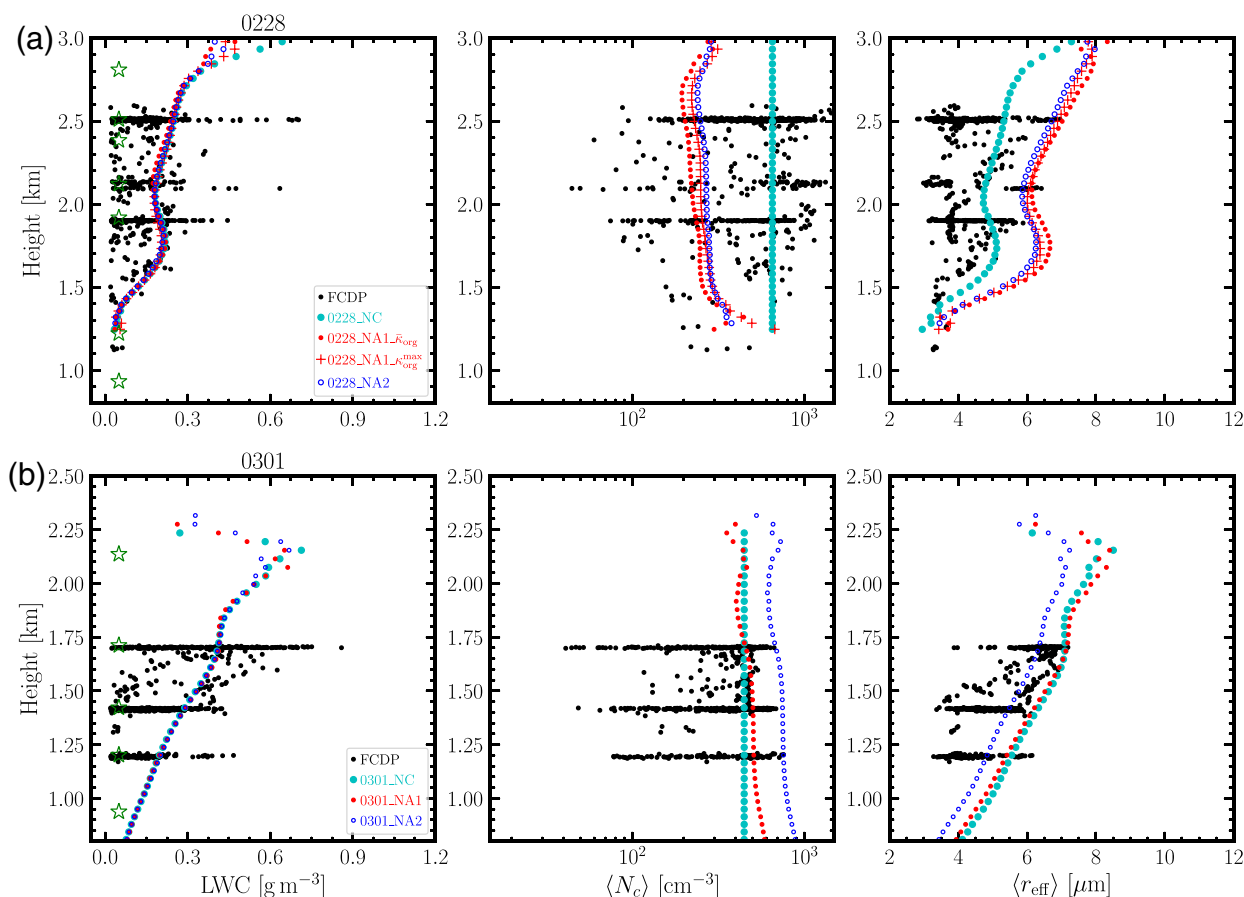| Simulations	N_a (cm^{-3})	N_c (cm^{-3})	BCB leg	$\overline{\kappa}$
0228_NC	—	650	—	—
0228_NA1_$\overline{\kappa}_{org}$	5593	—	BCB1	0.313
0228_NA1_κ_{org}^{max}	5593	—	BCB1	0.392
0228_NA2	5364	—	BCB2	0.341
0301_NC	—	450	—	—
0301_NA1	1434	—	BCB1	0.451
0301_NA2	3100	—	BCB2	0.479

FIG. 3. Comparison of vertical profiles of LWC, $\langle N_c \rangle$, and $\langle r_{eff} \rangle$ between LES and FCDP measurements for the (a) 28 Feb and (b) 1 Mar cases. A threshold of LWC = 0.02 g m^{-3}, 3.5 μm $\leq d_{eff} \leq$ 50 μm, and N_c = 20 cm^{-3} is applied to both the LES and FCDP (black dots) cloud averages. The measurement was taken during 1600–1700 UTC 28 Feb and 1500–1600 UTC 1 Mar 2020. The LES profiles are based on three snapshots 30 min apart. The green stars mark all the above cloud-base (ACB) and below cloud-top (BCT) flight legs.

case is characterized by warmer SST (SST = 293.25 K) and weaker turbulent surface heat fluxes (SHF = 79.91 W m^{-2} and LHF = 305.02 W m^{-2}) than those of the 1 March case (SST = 286.84 K, SHF = 231.76 W m^{-2}, and LHF = 382.18 W m^{-2}). For both cases, the magnitude of divergence is $\mathcal{O}(10^{-5})$ s^{-1} but a large-scale ascending motion for the 28 February case and subsidence for the 1 March case is imposed to the boundary layer during the analysis time. These conditions lead to a warmer, moister, and deeper boundary layer for the 28 February case than the 1 March case (Part I). The LES is able to capture the diurnal variation of the meteorological state (by comparing the LES to dropsonde measurements during the morning and afternoon flights) and cloud properties for both cases. Due to the strong forcing, clouds were well developed (quasi-steady LWP and cloud-top height) within the first 1–2 h after the spinup for the 1 March case. Clouds were developed gradually for the 28 February case. The LWP on 1 March is almost 3 times larger than that on the 28 February case. Snow and ice were observed for the 1 March case due to its colder BL. Both cases exhibit overcast cloudy conditions. We first compare the cloud microphysical properties between WRF-LES and FCDP measurements. Then,

aerosol effects on LWC, CFC, and radiation are investigated. Finally, we address how aerosols impact the BL meteorology.

a. Comparison of cloud microphysical properties

We start with control simulations with constant cloud droplet number concentration N_c (0228_NC and 0301_NC in Table 3), which are compared to simulations adopting prescribed aerosol size distributions derived from in situ measurements during different BCB flight legs. The constant N_c is the mean value from the FCDP measurements during the in-cloud legs of 28 February and 1 March cases. Figure 3 shows the comparison between WRF-LES and FCDP vertical profiles of LWC, $\langle N_c \rangle$, and $\langle r_{eff} \rangle$. For the 28 February case, simulations 0228_NC and 0228_NA1_$\overline{\kappa}_{org}$ yield almost the same LWC and different $\langle N_c \rangle$ and $\langle r_{eff} \rangle$ between 1600 and 1700 UTC. By examining the corresponding statistics shown in Fig. 4a at flight legs with sufficient statistics, it is evident that simulation 0228_NC is able to capture the vertical structure of $\langle N_c \rangle$ and $\langle r_{eff} \rangle$ while 0228_NA1_$\overline{\kappa}_{org}$ underestimates them compared to the FCDP measurements. The excellent agreement between simulation 0228_NC and the FCDP measurement is expected because the
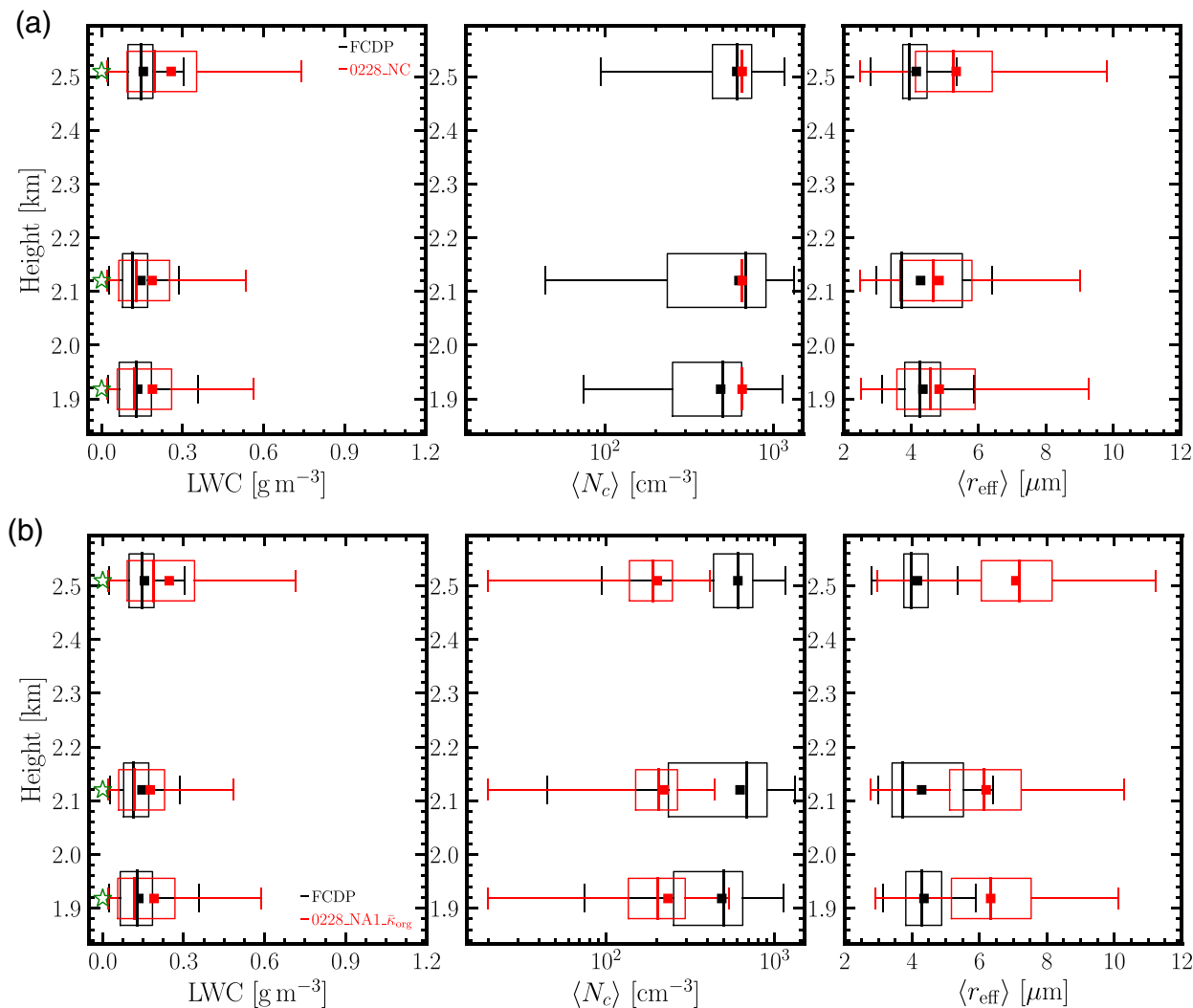
FIG. 4. Corresponding statistics of Fig. 3a for the 28 Feb case with (a) constant N_c (0228_NC) and (b) constant N_a (0228_NA1_$\overline{\kappa}_{org}$). Only the in-cloud flight legs (marked by green stars) that have sufficient data are used. The data are binned at those heights within ± 50 m. The height of the red box represents the bin width while the black box height is rescaled for readability. In the box-and-whisker plot, the binned data extend horizontally from the 25th to the 75th percentiles with the median and mean represented by the line inside the box and solid square, respectively. The minimum and maximum values are represented by the left and right end of whiskers, respectively.

mean N_c from the FCDP measurement is taken as the input for the LES. The underestimation of $\langle N_c \rangle$ from simulation 0228_NA1_$\overline{\kappa}_{org}$ is primarily due to the low total aerosol number concentration of the largest-size mode: $N_3 = 198$ cm^{-3} as listed in Table 1, which is about 3.3 times smaller than the FCDP-N_c.

The hygroscopicity of organic aerosols $\overline{\kappa}_{org}$ is difficult to determine due to uncertainties of their sources. We perform two simulations (0228_NA1_$\overline{\kappa}_{org}$ and 0228_NA1_κ_{org}^{max}) with the same prescribed aerosol size distribution but different $\overline{\kappa}$ (due to different $\overline{\kappa}_{org}$) estimated from the in situ aircraft measurements of mass of aerosol components during the ACTIVATE campaign for the 28 February case. As discussed in section 2b, we derive $\overline{\kappa}$ from either the mean or largest value of $\overline{\kappa}_{org}$. $\kappa_{org} = 0.1$, a mean value from Table 1 of Petters and Kreidenweis (2007), is

used to calculate $\overline{\kappa}$ for simulation 0228_NA1_$\overline{\kappa}_{org}$. In simulation 0228_NA1_κ_{org}^{max}, the upper value $\kappa_{org} = 0.229$ is adopted. As shown in Fig. 3, $\langle N_c \rangle$ and $\langle r_{eff} \rangle$ from simulation 0228_NA1_κ_{org}^{max} are almost identical to the ones from 0228_NA1_$\overline{\kappa}_{org}$. This is because κ of the organic component is about 6 times smaller than that of the inorganic components even though the mass fraction of the organic component is 54.5%.

We next investigate how vertical profiles of $\langle N_c \rangle$ and $\langle r_{eff} \rangle$ depend on different aerosol size distributions obtained from two BCB flight legs for the 28 February case. Simulation 0228_NA2 is the same as 0228_NA1_$\overline{\kappa}_{org}$ but with aerosol size distributions (Fig. 2b) and $\overline{\kappa}$ derived from BCB2 (Tables 1 and A2). Figure 3a shows that $\langle N_c \rangle$ and $\langle r_{eff} \rangle$ from simulation 0228_NA1_$\overline{\kappa}_{org}$ (red dots) are very close to the ones from 0228_NA2 (blue open circles), which is due to the fact that
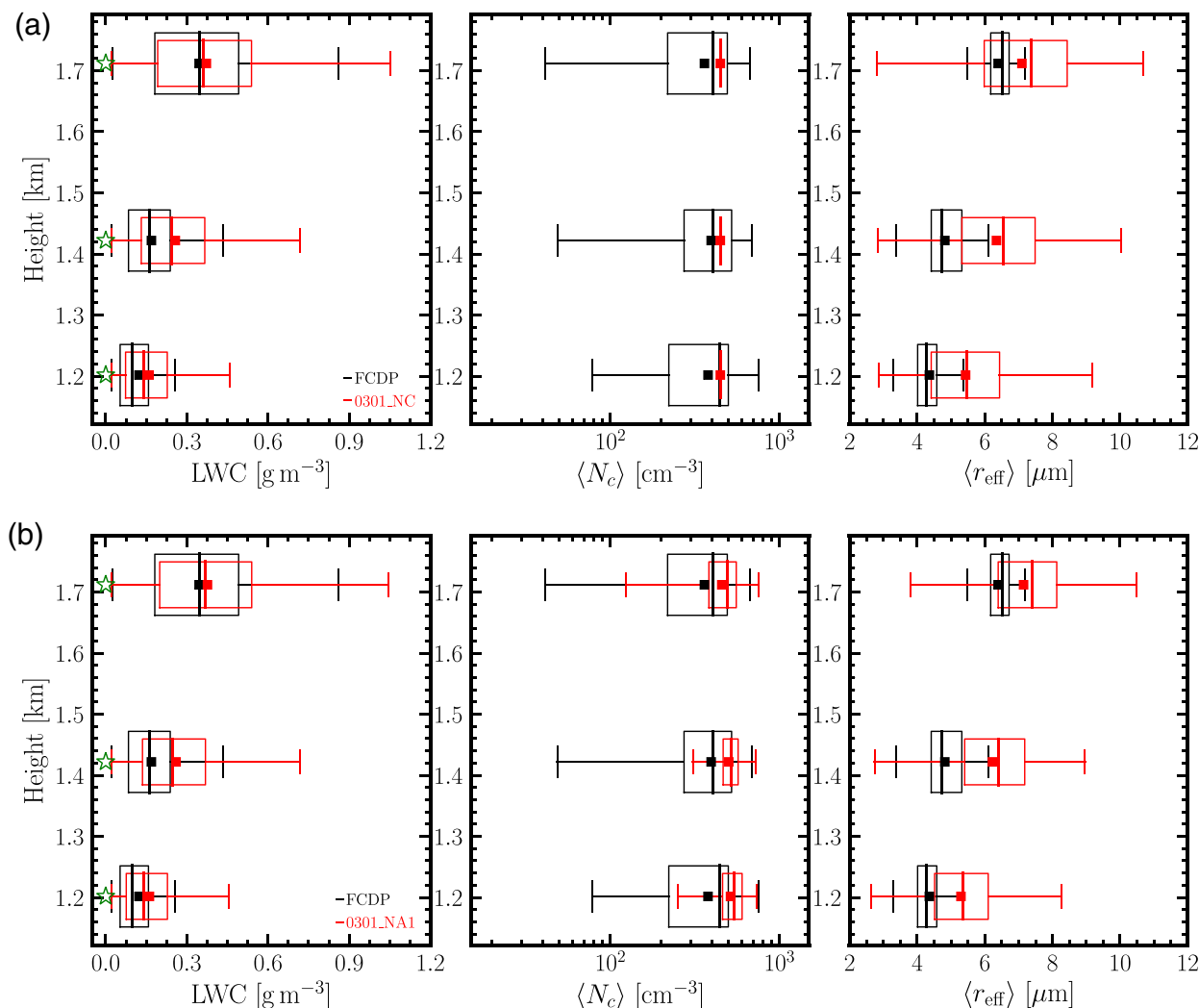
FIG. 5. As in Fig. 4, but for the 1 Mar case: simulation (a) 0301_NC and (b) 0301_NA1.

aerosol size distributions from the two BCB flight legs are similar as shown in Fig. 1. It is worth noting that the aerosol (LAS and SMPS) and FCDP measurements were not carried out simultaneously or collocated as shown in Fig. A2a for either BCB flight leg. Figure A1a shows the Falcon flight trajectory with the contour level representing the measurement time and stars and squares marking the start and end of BCB1 and BCB2 for the 28 February case. Most of the sampling of FCDP took place around 1624 UTC (Fig. A2a), which is closer to the BCB2 flight leg (Fig. A1a). This suggests that the location of aerosol measurements during BCB2 is closer to the FCDP measurement than that during BCB1, which explains why $\langle N_c \rangle$ and $\langle r_{eff} \rangle$ from simulation 0228_NA2 are slightly closer to FCDP values than those from 0228_NA1_$\bar{\kappa}_{org}$. Therefore, the discrepancy of $\langle N_c \rangle$ and $\langle r_{eff} \rangle$ between "NA" simulations and FCDP measurements likely depends on the collocation between the aerosol measurements and the FCDP measurements.

Figure 3b shows the comparison for the 1 March case. Vertical profiles from simulation 0301_NC are close to the ones from 0301_NA1. The statistics of vertical profiles from both simulation 0301_NC and 0301_NA1 agree well with the FCDP measurements as shown in Fig. 5 except for a slight overestimation of r_{eff}. We also perform a simulation with aerosol size distributions from BCB2 shown in Fig. 2b, with the number concentration of the largest size mode of which being about 2 times larger than the one from aerosol size distributions shown in Fig. 2a. As expected, $\langle N_c \rangle$ from simulation 0301_NA2 is larger than the one from 0301_NA1 as shown in Fig. 3b. This is because the BCB1 flight leg is collocated right below the FCDP data unlike the BCB2 flight leg as shown in Fig. A1b (the contour line between stars and the thick magenta line).

We also examine the diurnal variation of cloud properties by comparing the LES with the FCDP measurements during flights from 2047:07 to 2110:58 UTC and from 1943:30 to

2013:44 UTC for the 28 February and 1 March cases, respectively. LWC values from the LES and FCDP measurements agree well with each other (Figs. S1a and S2 in the supplement) for the 28 February case. N_c from the NA simulations capture the FCDP measurements better than the NC simulation. Interestingly, r_{eff} values from the FCDP measurements are captured well by the NC simulation between 1.7 and 2.5 km and are closer to NA simulations above 2.5 km. For the 1 March case, the LES captures the FCDP measurements well except that it slightly underestimates r_{eff} (Figs. S1b and S3 in the supplement). Overall, the LES is able to capture the diurnal variation of cloud properties.

b. Impact of different aerosol treatments on clouds and radiation

The comparison to in situ cloud observations indicates that the WRF-LES simulations can reasonably capture the vertical distribution of LWC in both CAO cases. Within the aerosol measurement uncertainties, the prescribed aerosol size distributions fed to WRF-LES show different impacts on N_c and other cloud properties when comparing the 28 February and 1 March cases. In both cases, the LWC exhibits very small sensitivity to different aerosol size distributions even though LWC varies greatly due to different SST, turbulent surface fluxes, and large-scale vertical velocity for the two cases. Therefore, changes in r_{eff} and N_c primarily reflect the impact of aerosols on droplet nucleation, similar to the first indirect effect. Due to colder SST (286.84 K) on the 1 March case compared to the 28 February case (293.25 K), ice particles were observed for the 1 March case but were barely detected for the 28 February case as shown in Fig. S4 in the supplement, where vertical profiles of IWC and $\langle N_{ice} \rangle$ from WRF-LES and 2DS measurements are shown, respectively. $r_{eff,ice}$ from 2DS sampling is also shown. Neither IWC nor $\langle N_{ice} \rangle$ are sensitive to aerosols in this case study. $\langle N_{ice} \rangle$ from the WRF-LES agrees reasonably well with the one from the 2DS sampling while IWC is off; however, the WRF-LES captures the higher magnitude of IWC on 1 March (see Fig. S5 in the supplement).

To quantitatively examine the sensitivity of cloud macrophysical properties (LWP, CFC, and IWP) and microphysical properties (N_c and r_{eff}) to the prescribed aerosols, we compare results between simulations with prescribed N_c and aerosol size distributions. To quantify the impact of prescribed aerosols on both the sign and the magnitude, we use the metric of percentage difference (PD), defined as PD $= (\mathcal{Q}_{NA} - \mathcal{Q}_{NC})/\mathcal{Q}_{NC} \times 100\%$ with $\mathcal{Q}_{NC}$ and $\mathcal{Q}_{NA}$ representing quantities from the NC (baseline) and NA simulations, respectively. $\mathcal{Q}$ is averaged between 1200 and 1800 UTC. For the 28 February case, we also assess the sensitivity of clouds and radiation to κ_{org}. The time evolution of differences in LWP, IWP, CFC, $\langle N_c \rangle$, $\langle r_{eff} \rangle$, and shortwave (SW) cloud forcing at the top of atmosphere (SW$_{TOA}$) between the control simulation 0228_NC and the ones with prescribed aerosol size distributions (0228_NA1_$\overline{\kappa}_{org}$, 0228_NA1_κ_{org}^{max}, and 0228_NA2) (based on different BCB flight legs) for the

28 February case is shown in Fig. 6. We first examine how much NA simulations differ from the NC simulation. LWP (Fig. 6a) from the NA simulations only changes slightly compared to the NC simulation (PD = −2.6%, 0.6%, and −0.5% for simulations 0228_NA1_$\overline{\kappa}_{org}$, 0228_NA1_κ_{org}^{max}, and 022_NA2, respectively) while IWP (Fig. 6c) decreases considerably (PD = −24.8%, −11.6%, and −12.4%). The CFC (Fig. 6b) increases slightly (PD = 1.4%, 0.9%, and 1.2%). N_c (Fig. 6d) decreases substantially (PD = −60.9%, −55.7%, and −55.0%). Correspondingly, $\langle r_{eff} \rangle$ (Fig. 6e) increases (PD = 27.2%, 23.8%, and 21.5%). ΔSW$_{TOA}$ (Fig. 6f) changes by 0.19, −0.94, and −0.93 W m^{-2} for simulations 0228_NA1_$\overline{\kappa}_{org}$, 0228_NA1_κ_{org}^{max}, and 0228_NA2, respectively.

To examine the effect of κ on these quantities, we compare simulation 0228_NA1_$\overline{\kappa}_{org}$ and 0228_NA1_κ_{org}^{max}. We use ΔPD $= (\mathcal{Q}_{NA_i} - \mathcal{Q}_{NC})/\mathcal{Q}_{NC}$ to quantify differences between NA simulations, where the subscripts NA$_i$ and NA$_j$ indicate two different NA simulations. ΔLWP from simulations 0228_NA1_$\overline{\kappa}_{org}$ (red solid circles in Fig. 6a) and 0228_NA1_κ_{org}^{max} (red pluses) starts to differ around 1000 UTC while ΔIWP starts to differ around 1500 UTC (Fig. 6c). The difference of PD between simulation 0228_NA1_κ_{org}^{max} and 0228_NA1_$\overline{\kappa}_{org}$ in LWP is ΔPD$_{LWP}$ = [0.63% − (−2.58%)] = 3.21%, while for IWP it is ΔPD$_{IWP}$ = 13.11%. However, ΔCFC is almost the same with ΔPD$_{CFC}$ = −0.50%. $\Delta\langle N_c \rangle$ and $\Delta\langle r_{eff} \rangle$ show considerable differences between simulations 0228_NA1_$\overline{\kappa}_{org}$ and 0228_NA1_κ_{org}^{max} with ΔPD$_{N_c}$ = 5.22% and ΔPD$_{r_{eff}}$ = −3.41%, respectively. ΔSW$_{TOA}$ decreases by 1.13 W m^{-2}.

How cloud properties respond to aerosol size distributions from different BCB flight legs is examined by comparing simulations 0228_NA1_$\overline{\kappa}_{org}$ (red solid circles) and 0228_NA2 (blue open circles) in Fig. 6, in which aerosol size distributions from BCB2 (listed in Table 1) are used. Minor differences are observed for ΔLWP (ΔPD$_{LWP}$ = 1.06%) while considerable differences are evident for ΔIWP (ΔPD$_{IWP}$ = 12.37%), $\langle N_c \rangle$ (ΔPD$_{N_c}$ = 5.85%) and $\langle r_{eff} \rangle$ (ΔPD$_{r_{eff}}$ = −5.74%). ΔCFC (ΔPD$_{CFC}$ = −0.20%) almost has no difference. However, the magnitude of the CFC vertical structure exhibits difference. ΔSW$_{TOA}$ decreases by 1.11 W m^{-2}. We further quantify the aerosol effect on radiative forcing by examining the response of cloud optical depth τ_c to cloud-top N_c via the following relation (Ghan et al. 2016),

$$\frac{\Delta\ln\overline{\tau_c}}{\Delta\ln\overline{\langle N_c \rangle}} = \frac{\Delta\ln\overline{LWP}}{\Delta\ln\overline{\langle N_c \rangle}} - \frac{\Delta\ln\overline{\langle r_{eff} \rangle}}{\Delta\ln\overline{\langle N_c \rangle}}. \quad (4)$$

Perturbations of LWP and cloud-top r_{eff} due to N_c (cloud top) are $\Delta\ln\overline{LWP}/\Delta\ln\overline{\langle N_c \rangle}$ = 0.150 and $\Delta\ln\overline{\langle r_{eff} \rangle}/\Delta\ln\overline{\langle N_c \rangle}$ = −0.269, respectively, which leads to $\Delta\ln\overline{\tau_c}/\Delta\ln\overline{\langle N_c \rangle}$ = 0.419 according to Eq. (4).

For the 1 March case, LWP (Fig. 7a) only changes slightly with PD = 0.06% and −0.02% for simulations 0301_NA1 and 0301_NA2 compared to simulation 0301_NC, respectively. PD of IWP (Fig. 7c) is −0.06% and 2.34%. The CFC (Fig. 7b) decreases with PD = −3.40% and −3.36%. The magnitude of the CFC vertical structure is quite similar. $\langle N_c \rangle$ (Fig. 7d) increases with PD = 12.80% and 70.06%. $\langle r_{eff} \rangle$ (Fig. 7e)
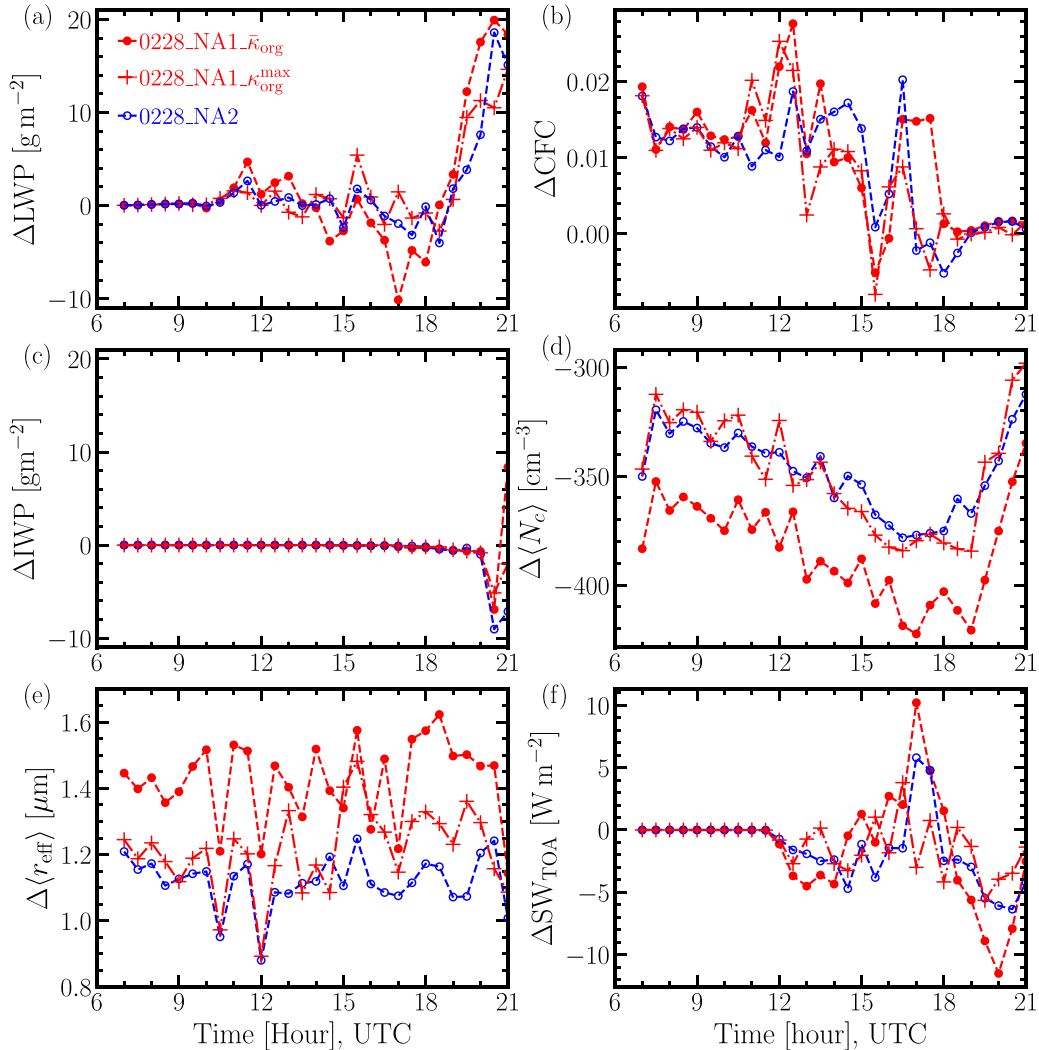
FIG. 6. Time series differences of LWP, CFC, IWP, $\langle N_c \rangle$, $\langle r_{\mathrm{eff}} \rangle$, and SW_{TOA} between the control simulation (0228_NC) and the ones (0228_NA1_$\bar{\kappa}_{\mathrm{org}}$, solid red circles; 0228_NA1_$\kappa_{\mathrm{org}}^{\max}$, red plus signs; 0228_NA2, open blue circles) with prescribed aerosol size distributions for the 28 Feb case. $\langle N_c \rangle$ and $\langle r_{\mathrm{eff}} \rangle$ are averaged within clouds with a threshold of $q_c \geq 0.02$ g kg^{-1}, which is also used to calculate cloud fractional coverage (CFC). LWP includes liquid water and rain. IWP includes ice, graupel, and snow.

decreases with PD = −1.77% and −12.77%. ΔSW_{TOA} (Fig. 7f) decreases by 1.24 and 0.51 W m^{-2}.

Similar to the 28 February case, ΔLWP ($\Delta PD_{\mathrm{LWP}} = -0.51\%$ between simulations 0301_NA2 and 0301_NA1) and ΔIWP ($\Delta PD_{\mathrm{IWP}} = 2.38\%$) on 1 March are slightly affected by different prescribed aerosol size distributions while CFC ($\Delta PD_{\mathrm{CFC}} = -0.15\%$) is insensitive to them. Aerosol size distributions are quite different (Fig. 2) between the two BCB legs (total N_a of the largest size from the flight leg BCB2 is about 2.16 times larger than that of BCB1) for the 1 March case, which leads to substantial differences in $\langle N_c \rangle$ ($\Delta PD_{N_c} = 57.26\%$) and $\langle r_{\mathrm{eff}} \rangle$ ($\Delta PD_{r_{\mathrm{eff}}} = -11.00\%$) as shown in Fig. 7. However, the difference between simulation 0301_NA2 and 0301_NA1 in ΔSW_{TOA} is only 0.72 W m^{-2}. Differences in aerosol size distribution induced susceptibility of LWP and cloud-top r_{eff} to N_c (cloud top) are

$\Delta \ln \overline{\mathrm{LWP}} / \Delta \ln \overline{\langle N_c \rangle} = -0.002$ and $\Delta \ln \overline{\langle r_{\mathrm{eff}} \rangle} / \Delta \ln \overline{\langle N_c \rangle} = -0.318$, respectively, which results in a positive perturbation of $\Delta \ln \overline{\tau_c} / \Delta \ln \overline{N_c}$ [Eq. (4)] of 0.316. The susceptibility of LWP and cloud-top r_{eff} to N_c (cloud top) for both cases is summarized in Table 4. The 28 February case yields $\Delta \ln \overline{\mathrm{LWP}} / \Delta \ln \overline{\langle N_c \rangle} = 0.15$, which is close to 0.11 reported in Lee et al. (2009) and summarized in Table S1 of Glassmeier et al. (2021). Our values are very different from other LES studies reported in Table S1 of Glassmeier et al. (2021), in which $\Delta \ln \overline{\mathrm{LWP}} / \Delta \ln \overline{\langle N_c \rangle}$ due to precipitation or entrainment were summarized. However, we note that both the 28 February and 1 March cases represent nonprecipitating stratocumulus clouds. It is very likely that $\Delta \ln \overline{\mathrm{LWP}} / \Delta \ln \overline{\langle N_c \rangle}$ is through the entrainment process in these two cases. The entrainment rate w_e (Figs. C1a,c) for both cases is an order of magnitude larger than that in previous studies
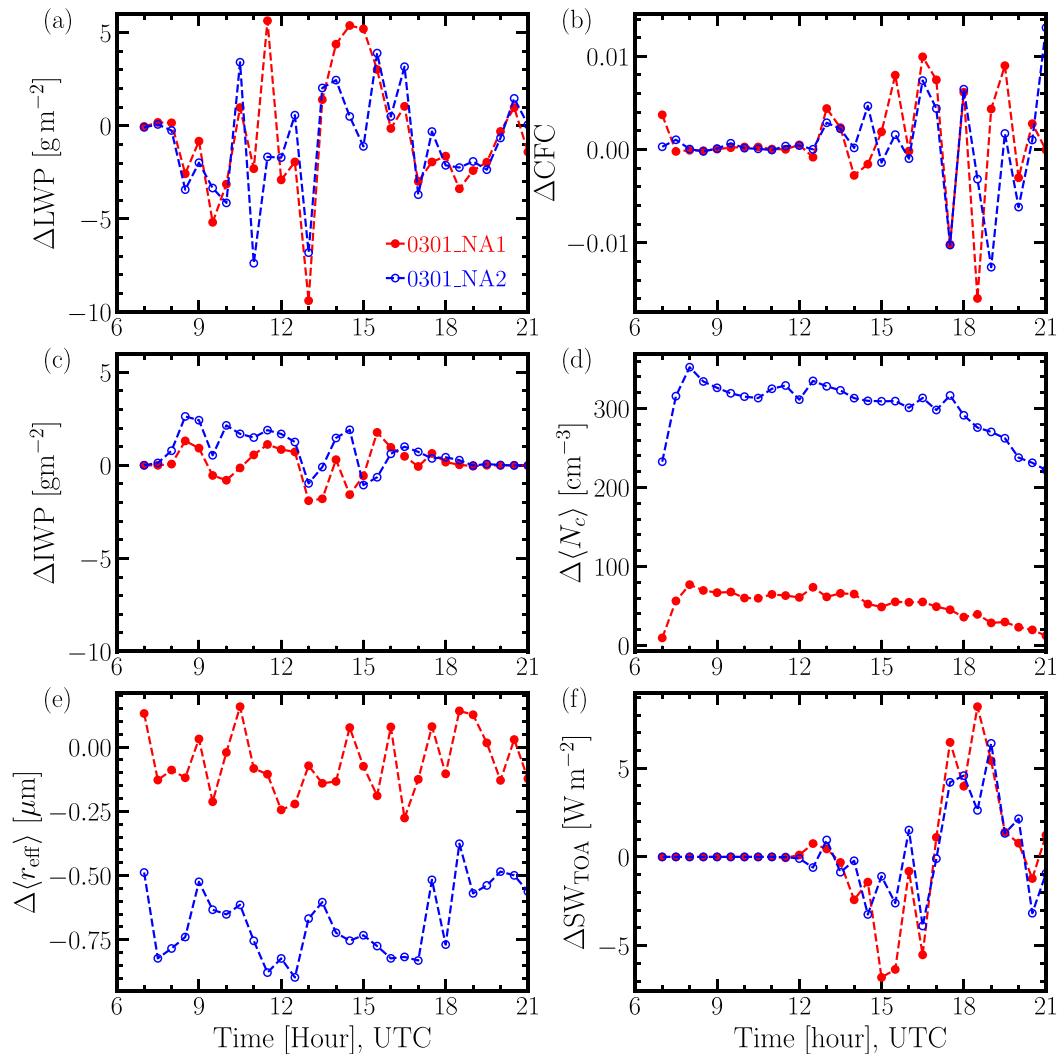
FIG. 7. As in Fig. 6, but for the 1 Mar case.

(e.g., Ackerman et al. 2009), likely due to the stronger large-scale vertical velocity and surface heat fluxes. Our w_e from the 1 March case is comparable to the one reported in Tornow et al. (2022), who used satellite retrievals and reanalysis data for the w_e estimate. For the 28 February case, w_e is strongly correlated with LWP with a Pearson correlation coefficient of 0.85, 0.89, and 0.88 (data from 1200 to 2030 UTC) and p value < 0.001 for the NC, NA1, and NA2 simulations, respectively. This indicates that the cloud-top entrainment process impacts LWP, as

expected for the nonprecipitating marine stratocumulus clouds (Glassmeier et al. 2021). Similar variability of w_e and correlation with LWP are seen in the 1 March case (Pearson correlation coefficient is 0.52, 0.57, and 0.53 with p value < 0.03 for the NC, NA1, and NA2 simulations, respectively). w_e responds differently to aerosol perturbations in the two cases and the responses vary with time (Figs. C1b,d). Although the time-varying large-scale vertical velocity profile (based on ERA5 forcing) is the same for the different simulations of each case, Δw_e, which is primarily determined by changes in cloud-top height, can be influenced by the large-scale forcings as well as thermodynamical/radiative feedback from the aerosol impact on cloud microphysical properties. This challenge warrants a dedicated investigation. Overall, these two case studies show that spatial–temporal variation of aerosol distributions have a profound effect on $\langle N_c \rangle$ and $\langle r_{\text{eff}} \rangle$. The effects on ΔLWP, ΔIWP, and ΔCFC are less obvious.

TABLE 4. Aerosol size distribution induced susceptibility of LWP and cloud-top r_{eff} to N_c (cloud top) for the 28 Feb (0228_NA2 − 0228_NA1_$\bar{\kappa}_{\text{org}}$) and 1 Mar (0301_NA2 − 0301_NA1) cases.

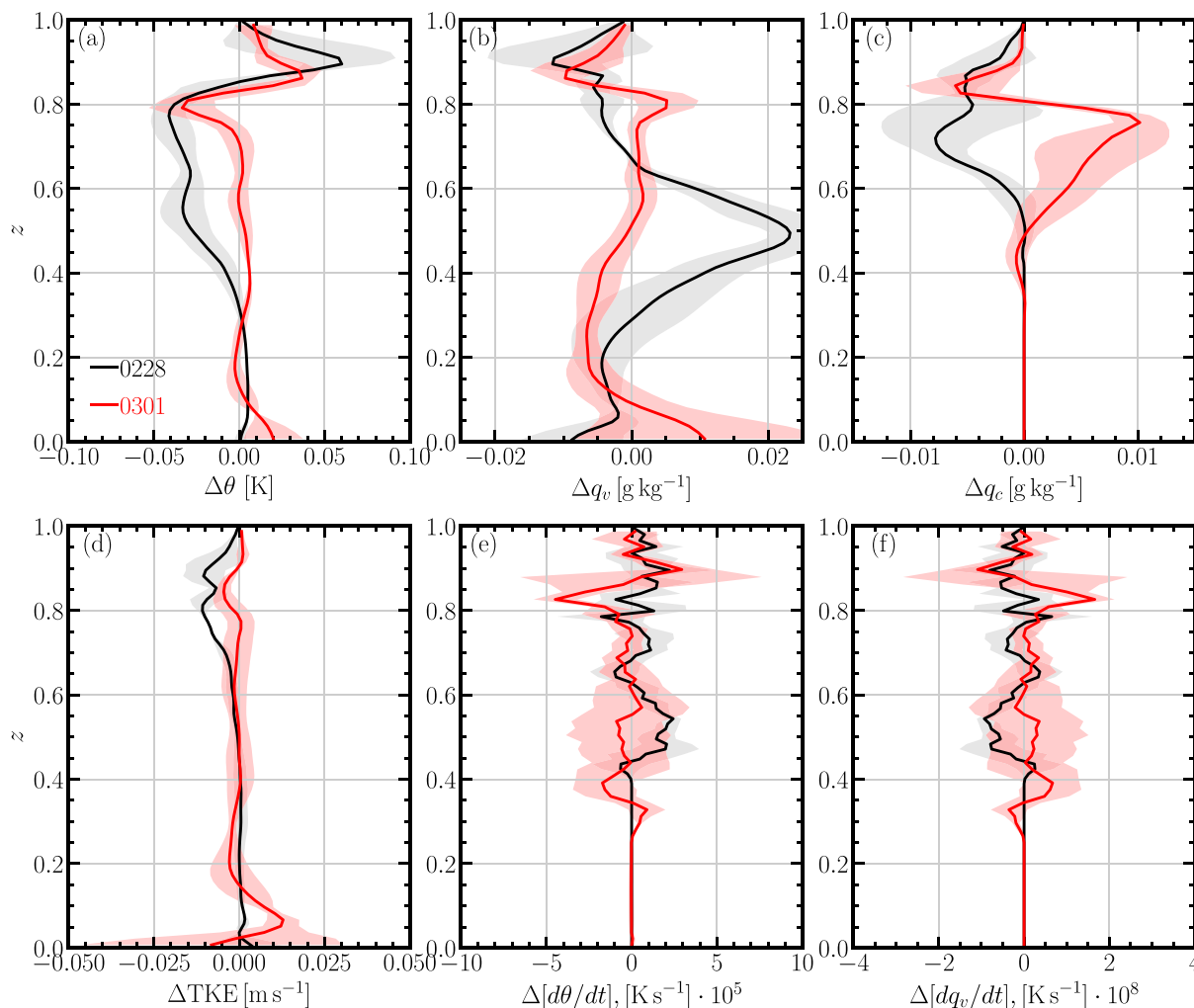| Case	$\Delta\ln\overline{\text{LWP}}/\Delta\ln\overline{\langle N_c \rangle}$	$-\Delta\ln\overline{\langle r_{\text{eff}} \rangle}/\Delta\ln\overline{\langle N_c \rangle}$	$\Delta\ln\overline{\tau_c}/\Delta\ln\overline{\langle N_c \rangle}$
28 Feb	0.150	0.269	0.419
1 Mar	−0.002	0.318	0.316

FIG. 8. Difference of vertical profiles between simulation 0228_NA1_$\overline{\kappa}_{\text{org}}$ and 0228_NC (black curves) and between 0301_NA1 and 0301_NC (red curves) averaged during the dropsonde measurement time (1600–1700 UTC for the 28 Feb case and 1500–1600 UTC for the 1 Mar case) with the shading indicating $\pm\sigma$; z is the normalized height by the cloud-top height.

c. Impact of ACI on the boundary layer meteorology

In this section, we examine how aerosols impact BL meteorology for these two contrasting CAO cases. Differences of vertical profiles averaged within the corresponding dropsonde circle between NA and NC simulations are shown in Fig. 8, where z is the altitude normalized by the cloud-top height. We take simulations 0228_NA1_$\overline{\kappa}_{\text{org}}$ and 0301_NA1 as an example. For both cases, simulations with prescribed aerosol size distributions yield larger θ (red and black curves in Fig. 8a) and smaller q_v (Fig. 8b) near the inversion top due to the enhanced $d\theta/dt$ (Fig. 8e) and weakened dq_v/dt (Fig. 8f) by condensation/evaporation, but there are quite different responses near cloud base between the two cases. This demonstrates that aerosol affects meteorological states via the case-dependent response in cloud condensation/evaporation processes to aerosol perturbations as were also shown in previous studies, e.g., Andrejczuk et al. (2010). Even for the

same case (0228 or 0301), different aerosol perturbations (0228_NA2 or 0301_NA2) have varying impacts on the cloud and thermodynamical processes, in terms of magnitude and vertical location compared to those of 0228_NA1 and 0301_NA1, correspondingly. The response evolves with time as well. For the 28 February case, simulation 0228_NA1_$\overline{\kappa}_{\text{org}}$ yields smaller N_c (negative $\Delta\langle N_c \rangle$ shown by red dots in Fig. 6d) and correspondingly, larger SW$_{\text{TOA}}$ compared to 0228_NC between 1600 and 1700 UTC (positive ΔSW$_{\text{TOA}}$ shown by red dots in Fig. 6f), which contributes to a warmer but drier cloud top as shown by the black curve ($z \geq 0.85$) in Figs. 8a and 8b. q_v is positively correlated to TKE within clouds due to turbulent transport and mixing. The same conclusion is drawn for the 1 March case. We also examine the time evolution of vertical-profiles difference for the 28 February case (see Fig. S11 in the supplement). The aerosol effect on θ at the inversion layer evolves from positive to negative and stays positive within the boundary layer. In contrast, an opposite response is observed for the aerosol effect

on q_v and q_c. Unlike the 28 February case, the positive effect on θ and negative effect on q_v and q_c of aerosols persists to the end of the simulation and is more profound near the evolving simulation and is stronger near the evolving cloud top as discussed for the 1 March case (see Fig. S12 in the supplement). $\Delta d\theta/dt$ and $\Delta dq_v/dt$ due to condensation shows the most distinct structure at the cloud top and the cloud base. The response of TKE vertical profiles to aerosols is more complicated. It exhibits strong spatial variations for both 28 February and 1 March cases. For both cases, the strongest response of TKE occurs near the cloud top due to the radiative cooling. A negative ΔSW_{TOA} strengthens the TKE and vice versa as can be seen from the evolution of ΔSW_{TOA} (Figs. 6f and 7f) and TKE vertical profiles (Figs. S11 and S12 in the supplement). Since the turbulent surface fluxes and large-scale forcings (θ and q_v tendencies and the vertical motion) for the NA and NC simulations are the same, we can faithfully conclude that ACI affects the BL thermodynamics and clouds via the radiative cooling process due to aerosol perturbations.

5. Evaluating cloud micro-/macroproperties in ERA5 and MERRA-2

One goal of the present study, which is also part of the overall objective of the ACTIVATE field campaign, is to evaluate and improve the representation of MBL clouds and cloud–aerosol interactions in GCMs using process studies constrained by the field measurements. As a first step to approaching this goal, we evaluate large-scale model reanalysis products that have assimilated observational data (not including the ACTIVATE measurements) against the high-resolution model results constrained and/or validated by the ACTIVATE measurements. Such an evaluation is feasible and meaningful because the WRF-LES model domain is comparable to the grid size of ERA5 and MERRA-2. In addition, the initial conditions and large-scale forcings (i.e., advective tendencies and surface fluxes) for the LES simulations are taken from the reanalysis products. Thus, the comparison can focus on the importance of resolved turbulence, aerosol activation, and other small-scale cloud processes. In this section, we evaluate ERA5 and MERRA-2 data by comparing the LWP, CFC, N_c, and r_{eff} from LES and *GOES-16* to those from ERA5 and MERRA-2 data. Both ERA5 and MERRA-2 provide LWP as part of their hourly single-level data. The CFC field of ERA5/MERRA-2 is defined as the maximum cloud fraction in the vertical (up to 7 km) based on the model-level LWC data with a threshold of LWC = 0.02 g cm^{-3} for cloud. Note that ERA5 and MERRA-2 provide 1-hourly and 3-hourly data (instantaneous field) for the CFC calculation, respectively. The *GOES-16* LWP is corrected using the mean bias reported in Painemal et al. (2012, 2021a).

Figure 9 shows the comparison between LES, *GOES-16*, ERA5, and MERRA-2 for the 28 February case. LWP (Fig. 9a) and CFC (Fig. 9b) retrieved from *GOES-16* agree reasonably well with the LES, which boosts our confidence to evaluate the ERA5 and MERRA-2 using LES. Compared to simulation 0228_NA1_$\bar{\kappa}_{\text{org}}$, ERA5 slightly overestimates the LWP while MERRA-2 underestimates it. Nevertheless, both ERA5 and MERRA-2 capture the time evolution of LWP

well. MERRA-2 has a significantly lower CFC compared to the LES, while CFC has an opposite time evolution between ERA5 and LES. We further compare the evolution of vertical structure of LWC and CFC between ERA5, MERRA-2, and LES. As shown in Fig. 10, MERRA-2 underestimates the magnitude of CFC and LWC compared to the LES. Neither MERRA-2 nor ERA5 captures the vertical structure of CFC and LWC of LES that has an apparent peak near cloud top.

We also compare N_c and r_{eff} retrievals from *GOES-16* with the LES near the top of clouds. *GOES-16* N_c is derived from cloud effective radius in μm and cloud optical depth τ under the adiabatic assumption. The adiabatic lapse rate of condensation Γ (g m^{-4}) is estimated from the cloud-top temperature and pressure retrievals from *GOES-16* (see appendix B for details of the estimation). Since several studies have shown the presence of a systematic positive bias in satellite-based r_{eff} (Painemal et al. 2012; Noble and Hudson 2015; Zhang et al. 2017; Painemal et al. 2021a), here we use values reported in Painemal et al. (2012, 2021a) for *GOES-13* and *GOES-16* to correct r_{eff} and, in turn, correct N_c via Eq. (B1). To be consistent with the sensitivity of satellite r_{eff} to the cloud's uppermost layer, N_c and r_{eff} from WRF-LES are averaged over the cloud top (four layers, about 150 m). Figures 9c and 9d show that N_c and r_{eff} from WRF-LES with constant N_c agree reasonably well with those from *GOES-16*.

Figure 11 shows the comparison between LES, *GOES-16*, and reanalysis for the 1 March case. The agreement in both magnitude and variation of LWP and CFC between the LES and *GOES-16* is reasonably good. Compared to the LES and *GOES-16*, both MERRA-2 and ERA5 underestimate LWP. However, ERA5 agrees better with the LES in the diurnal variation. ERA5 agrees with LES in CFC while MERRA-2 underestimates CFC. The vertical profiles of LWC and CFC are shown in Fig. 12. Similar to the 28 February case, neither ERA5 nor MERRA-2 capture the vertical structure of CFC compared to LES. Nevertheless, they exhibit comparable vertical structure of LWC to the LES. ERA5 has larger CFC (nearly overcast condition) near cloud base and an LWC maximum in the middle of cloud layers. MERRA-2 has the lowest LWC and CFC at all heights. *GOES-16* gives a similar N_c and r_{eff} compared to LES at the cloud top.

6. Discussion and conclusions

Using the WRF-LES, we have simulated two cold-air outbreak (CAO) cases (28 February and 1 March 2020) observed during the ACTIVATE campaign in the western North Atlantic Ocean. The aerosol–meteorology–cloud interaction (AMCI) during the two CAO events are examined by comparing WRF-LES, measurements, satellite retrievals, and reanalysis.

Aerosol size distributions measured from airborne sampling are prescribed to the LES experiments, which are compared to previous experiments with prescribed cloud droplet number concentrations (Part I). Cloud properties from the LES experiments are then validated against the FCDP in situ measurements. Lognormal aerosol size distributions are fitted from data acquired during two below cloud-base (BCB) flight legs for each case. Bulk aerosol hygroscopicity estimated
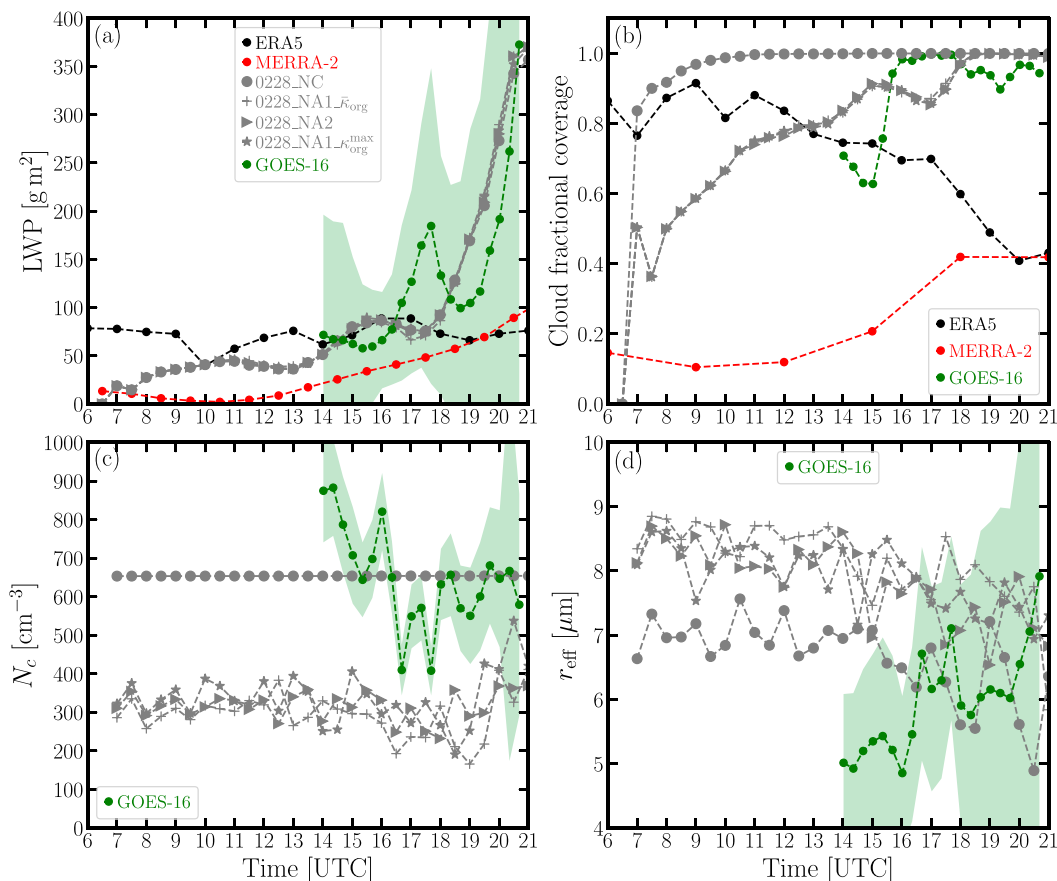
FIG. 9. Comparison between the WRF-LES (gray), ERA5 (black), MERRA-2 (red), and *GOES-16* (green with $\pm\sigma_\epsilon$ uncertainty) for the 28 Feb case. The gray dashed lines with symbols represent individual simulations. LWP is hourly for ERA5 and MERRA-2. CFC for both ERA5 (hourly) and MERRA-2 (3 hourly) represents the maximum low cloud cover among the vertical levels, defined with a threshold of LWC = 0.02 g cm^{-3}. LES N_c and r_{eff} are averaged over the cloud top (four layers). All the ERA5, MERRA-2, and *GOES-16* data are averaged over the dropsonde area. LWP, N_c, and r_{eff} from *GOES-16* are filtered by cloud optical depth $\geq$ 3. *GOES-16* CFC represents the fraction of pixels with LWP or IWP $\geq$ 0 within the dropsonde measurement area. To reduce the well-known systematic retrieval biases, the *GOES-16* LWP is corrected by the mean of the lower +10 g m^{-2} and upper +19 g m^{-2} bias bounds reported in Painemal et al. (2012, 2021a). The *GOES-16* r_{eff} [N_c according to Eq. (B1)] are corrected by the mean of lower −2.4 μm and upper −4.0 μm bias bounds according to Painemal et al. (2012, 2021a). *GOES-16* data before 1400 UTC are excluded because the retrievals are less reliable for low solar angles.

from the mass of individual aerosol components measured by the Aerodyne Mass Spectrometer is used in the LES. For organic species, we need to make assumptions in the component hygroscopicity. To examine the effect of aerosols, we compared LES results with prescribed aerosol size distributions from different flight legs and/or with different assumptions in the estimation of bulk hygroscopicity (denoted as NA-LES) to the ones with constant cloud droplet number concentration N_c (denoted as NC-LES) obtained from the FCDP sampling. For the 28 February case, vertical profiles of LWC from the two NA-LES are in good agreement. However, N_c (r_{eff}) from the NC-LES is larger (smaller) than that from NA-LES. This is speculated to be because the aerosol sampling during the two BCB legs were not collocated very well with the FCDP sampling in space. For the 1 March case, LWC, N_c, and r_{eff} from NC-LES agree better

with those from NA-LES using aerosol size distributions derived from the BCB flight leg that collocated well in space with the FCDP cloud droplet sampling. Our LES–measurement comparison also demonstrates a strong spatial and temporal variation of aerosol size distributions during the CAO events, which adds challenges to LES modeling and validation. We note that simulations with the prescribed cloud droplet number is supposed to match the FCDP measurements the best as the measured mean N_c from FCDP is used as the input for the LES. However, our goal here is to explore AMCI associated with CAO over the WNAO region with realistic forcing from the ACTIVATE measurements and reanalysis instead of finding the best LES input and assumption to reproduce the measurements. By comparing LES to the measurements during flights on the same day but at a later time, we show that
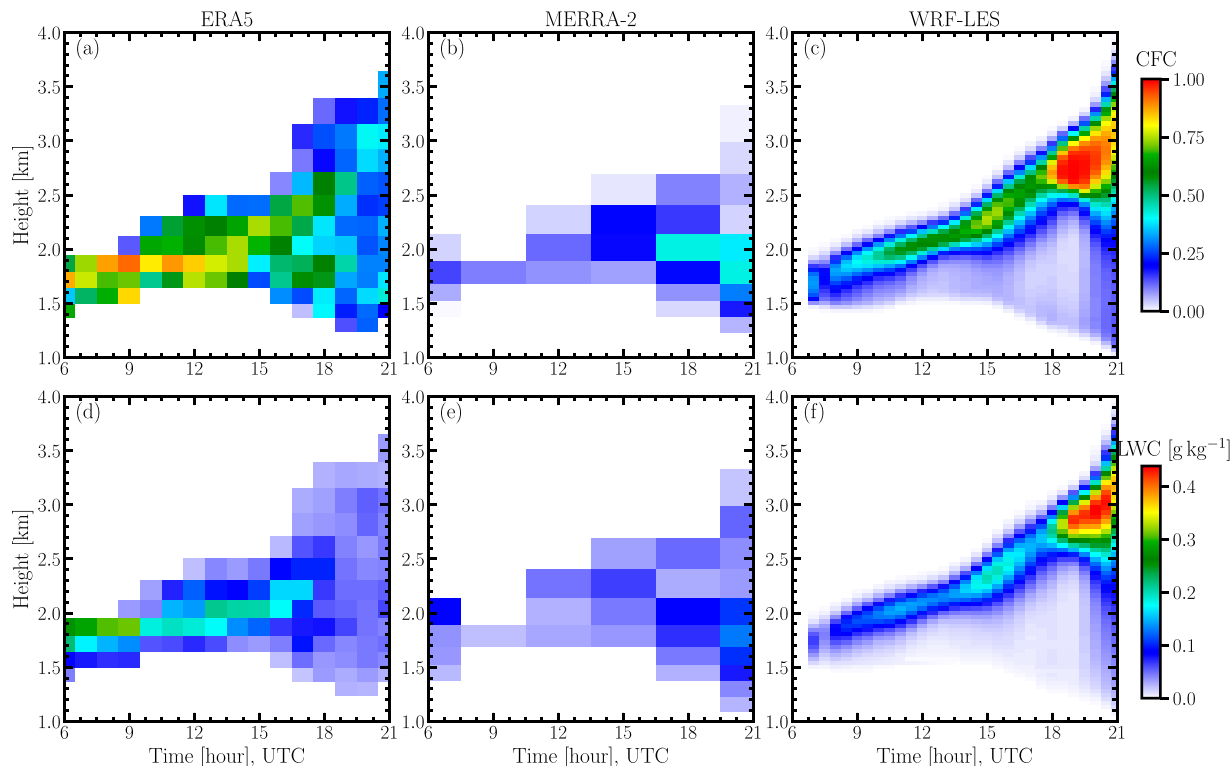
FIG. 10. Evolution of vertical profile of cloud coverage and LWC for the 28 Feb case, defined with a threshold of LWC = 0.02 g cm^{-3}. ERA5 and MERRA-2 data are averaged over the dropsonde area. WRF-LES shows the average of four simulations as in Fig. 9.

the LES captures the diurnal variation of cloud properties for both cases. Overall, the good agreement between WRF-LES and measurements gives us confidence to use the LES results to study the AMCI and evaluate reanalysis for the two CAO events.

Aerosol effects on cloud microphysical (N_c, and r_{eff}) and macrophysical properties (LWP and CFC) are investigated by comparing LES with aerosol size distributions from different BCB flight legs as input. Our use of measured aerosol size distributions to study the aerosol effects on cloud properties better represents aerosol perturbations in the study domain, which is more realistic compared to other LES studies with prognostic N_c but idealized aerosol size distributions. More importantly, LES with the same configuration and boundary/surface forcings but different aerosol perturbations allows us to investigate the aerosol effect on clouds excluding the meteorological variations, which is challenging in understanding ACI (Stevens and Feingold 2009). For the 28 February case, N_c and r_{eff} are influenced by aerosols via aerosol hygroscopicity $\overline{\kappa}$ and aerosol size distributions. With the same aerosol size distributions, increasing $\overline{\kappa}$ from 0.313 to 0.392 leads to a 5.2% increase (3.4% decrease) of N_c (r_{eff}). The top-of-the-atmosphere shortwave radiation SW$_{TOA}$ decreases by 1.13 W m^{-2}. LWP (IWP) increases by 3.2% (13.1%). The CFC only increases by 1.4%. Even though aerosol size distributions from two BCB legs are quite similar, a difference of 1.11 W m^{-2} in SW$_{TOA}$ is observed for the two simulations. For the 1 March

case, SW$_{TOA}$ only changes by 0.72 W m^{-2} when N_a differs by a factor of about 2.6 between two BCB flight legs. The effect of N_a on LWP and CFC is negligible. Aerosols impact the boundary layer structure via interactions with clouds and subsequent changes in latent heating, radiative cooling, and feedback from turbulence kinetic energy for the two cases. For example, for the 28 February case, the aerosol perturbation (e.g., increased bulk particle hygroscopicity) leads to stronger cloud radiative cooling, which results in colder θ and larger TKE and q_v. Due to the same external forcing of turbulent surface heat fluxes and large-scale advection but different aerosol perturbations in our LES, we are able to quantify the aerosol effect on thermodynamics and TKE via cloud changes. The aerosol impact on boundary layer structure was also investigated in previous studies using idealized forcings and aerosol size distributions (e.g., Andrejczuk et al. 2010), which may overestimate the significance of aerosol–cloud feedback due to aerosol perturbations as argued in Dagan et al. (2022). Therefore, the use of realistic forcing and aerosol size distributions from in situ measurement in our simulations can provide more realistic aerosol impact on boundary layer structure.

As we aim to eventually evaluate and improve AMCI processes in Earth system models using LES experiments informed by the ACTIVATE observations, we have also compared our LES results to satellite retrievals (*GOES-16*) and reanalysis products, such as ERA5 and MERRA-2. For
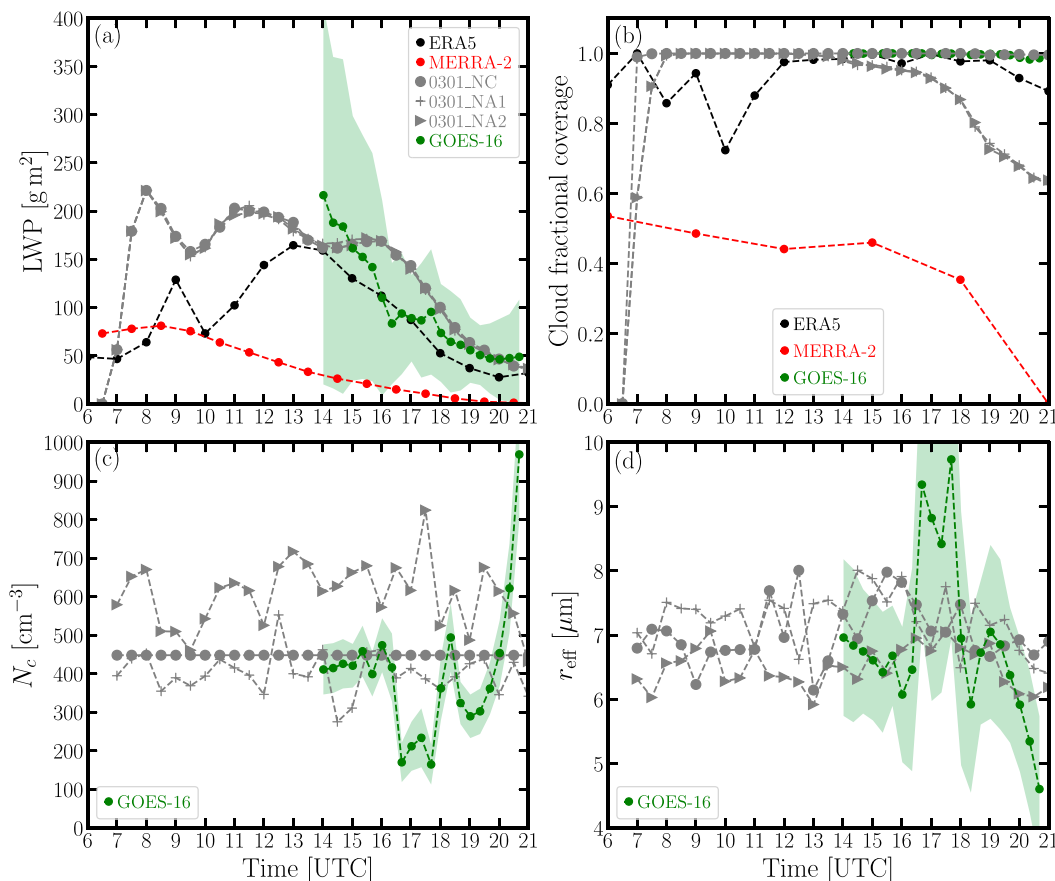
FIG. 11. As in Fig. 9, but for the 1 Mar case.

the 28 February case, LES and *GOES-16* agree reasonably well for LWP and CFC. ERA5 captures the LWP compared with LES while MERRA-2 slightly underestimates LWP. Time evolution and the magnitude of CFC among LES, ERA5, and MERRA-2 are quite different. Both ERA5 and MERRA-2 fail to capture the vertical structure of LWC and CFC compared to the LES. For the 1 March case, LES agrees well with *GOES-16* for LWP and CFC. Both ERA5 and MERRA-2 underestimate the LWP compared to LES, even though the time evolution of LWP exhibits a similar trend between ERA5 and the LES. ERA5 and LES agree well in the magnitude of CFC while MERRA-2 largely underestimates it. Similar to the 28 February case, the vertical structure of LWP and CFC from MERRA-2 and ERA5 are quite different from the LES. We have also validated N_c and r_{eff} from the LES against the *GOES-16* retrievals. For both cases, N_c and r_{eff} from the LES agree well with those from *GOES-16*. The horizontal grid spacing of $dx = 300$ m in our LES might be too coarse to adequately resolve turbulent eddies that are important for cloud formation and the wave features of roll clouds (e.g., Lai et al. 2020). Therefore, the conclusion of the present study may be dependent on the horizontal grid spacing, which will be explored in the future.

To the best of our knowledge, this is the first time such process-oriented modeling study of the AMCI has been performed for cold-air outbreaks with realistic aerosol perturbations and large-scale forcings from the ACTIVATE campaign measurements over the WNAO region. This study provides process-level understanding of AMCI during cold-air outbreak and makes a step further to demonstrate the use of field measurements and associated challenges in evaluating the representation of AMCI in Earth system models. For example, the estimated bulk hygroscopicity of aerosols (κ) and representation of aerosol size distributions, including the mass fraction of different components, are highly uncertain in GCMs. Using the estimated $\overline{\kappa}$ and aerosol number concentrations (N_a) based on the available in situ measurements of particle sizes and aerosol component mass, we show the sensitivity of N_c, r_{eff}, and liquid water path (LWP) to assumptions (e.g., $\overline{\kappa}$ derived from a range of κ values for the organic component and mean κ values for inorganic components) commonly used for estimating $\overline{\kappa}$ and N_a in the GCMs. This points to a new direction to reducing uncertainties in the parameterizations of AMCI processes in GCMs. To use the LES results to evaluate AMCI in Earth system models, the next step will be to simulate these two cases using a single-column configuration of Earth system models
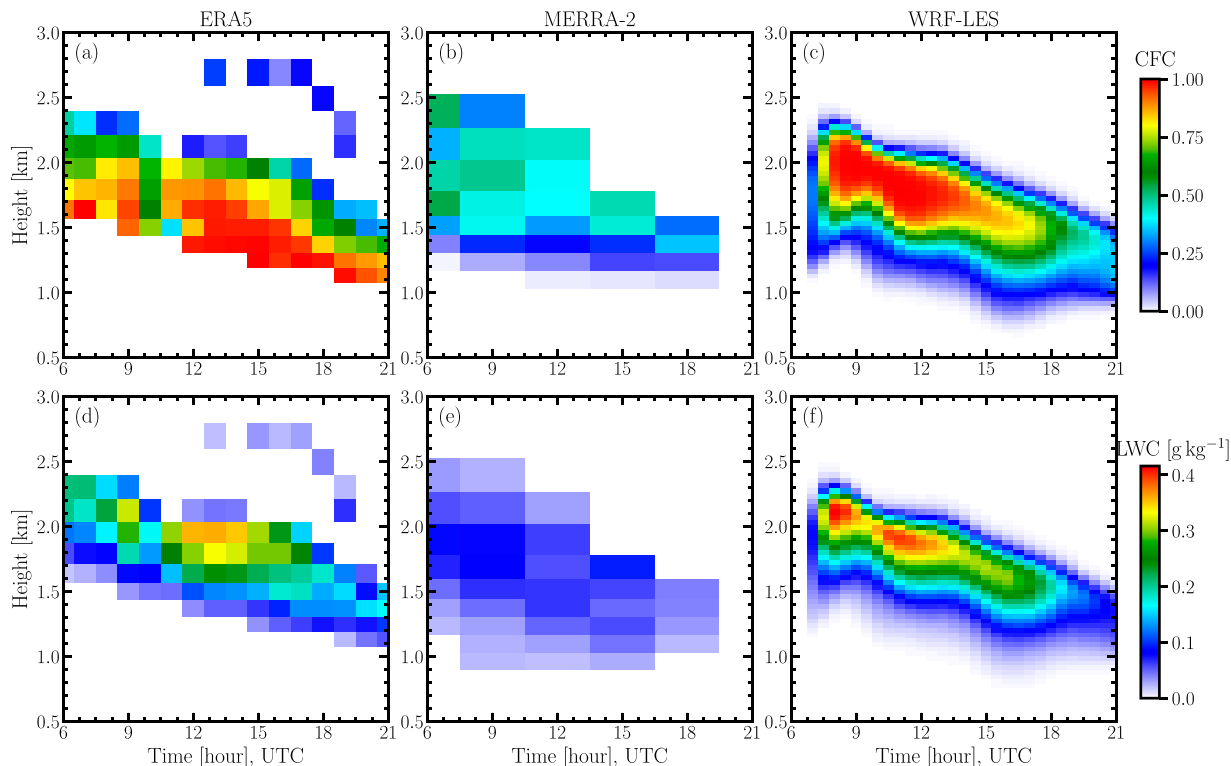
FIG. 12. As in Fig. 10, for the 1 Mar case. WRF-LES shows the average of three simulations as in Fig. 11.

driven by the same boundary and surface forcings obtained from ACTIVATE measurements and reanalysis products.
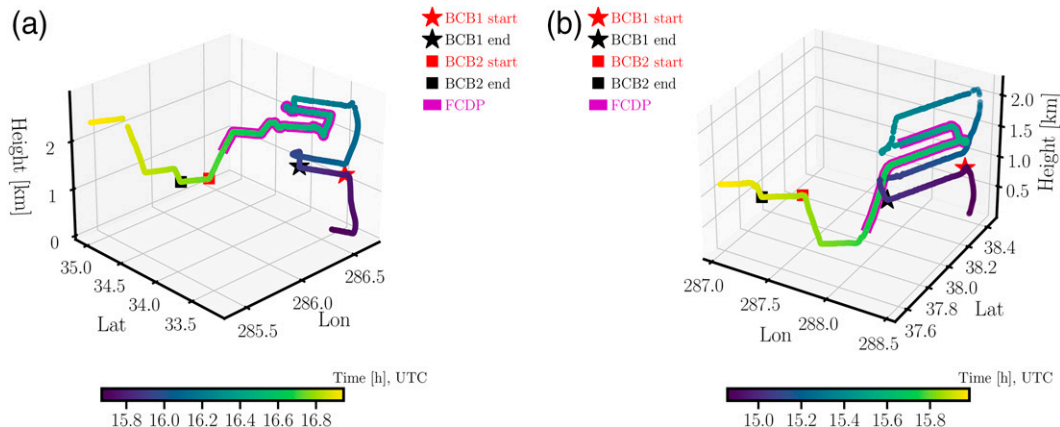
FIG. A1. Flight trajectory corresponding to the FCDP measurements for (a) the 28 Feb and (b) 1 Mar cases. Red and black stars (squares) represent the start and end of the BCB1 (BCB2) flight leg, respectively. Trajectories with densest FCDP sampling (16.3–16.7 and 15.45–15.75 UTC for the 28 Feb and 1 Mar cases, respectively) are highlighted as thick magenta curves.
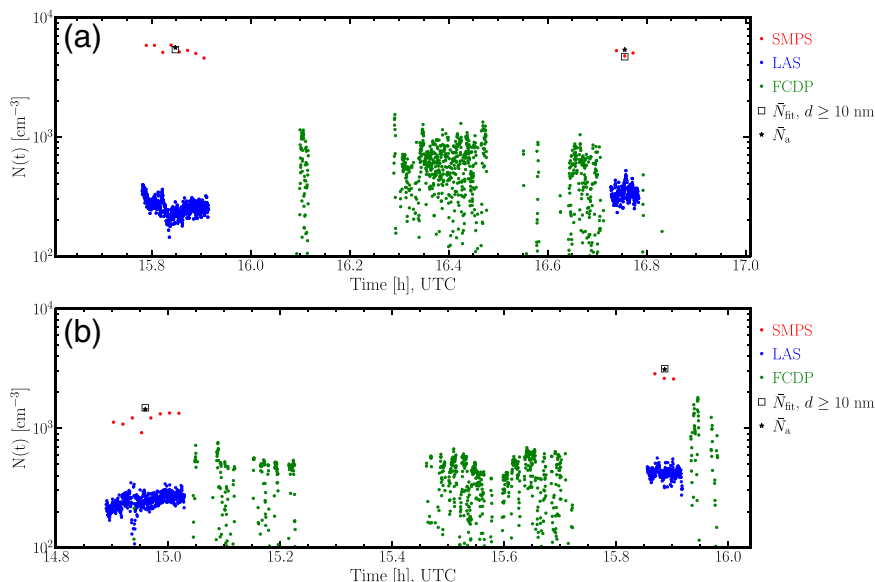
FIG. A2. Comparison between $\overline{N}_a$ (black star), $\overline{N}_{\text{fit}}$ (black square), and N_{FCDP} (green dots) for the (a) 28 Feb and (b) 1 Mar cases. Red and blue dots represent N_a from SMPS and LAS measurements, respectively.

simulations were performed using resources available through Research Computing at PNNL.

Data availability statement. ACTIVATE data are publicly available at http://doi.org/10.5067/SUBORBITAL/ACTIVATE/DATA001.

APPENDIX A

Validation of Lognormal Fitting of Aerosol Size Distributions

The 3D flight trajectories of the BCB legs for both cases are shown in Fig. A1. Figure A2 shows time series of measured particle number concentration of aerosols (SMPS and LAS) and cloud droplets (FCDP) during the two BCB legs for both cases. The SMPS measurements are free from spikes, indicative of no cloud artifacts (e.g., the cloud shattering) during the

TABLE A1. Time-averaged mass concentration $\overline{m_i}$ from the AMS measurement sampled during BCB flight legs for the 28 Feb (0228) and 1 Mar (0301) cases. NaCl is not efficiently sampled by AMS because it is refractory (i.e., not volatile at 600 Pa), and therefore, the Cl^{-1} mass is likely not representative of NaCl mass. It is justified by the lack of coarse-mode number concentration in Figs. 1 and 2.

Component	Organic	Sulfate (SO_4^{2-})	Nitrate (NO_3^-)	Ammonium (NH_4^+)
0228				
BCB1	54.5%	23.4%	10.8%	10.0%
BCB2	48.6%	25.9%	10.8%	13.9%
0301				
BCB1	27.6%	46.6%	3.4%	21.3%
BCB2	24.9%	28.5%	23.2%	22.6%

measurements. The validation of the lognormal fitting of aerosol size distributions is discussed in section 2a. Tables A1 and A2 show the AMS-measured mass concentration and the corresponding derived $\overline{\kappa}$, respectively, for the two cases.

APPENDIX B

Retrieve N_c and r_{eff} from *GOES-16*

GOES-16 N_c is derived from cloud effective radius (in μm) and cloud optical depth τ under the adiabatic assumption (Painemal and Zuidema 2011):

$$N_c = \Gamma^{1/2} \frac{10^{1/2}}{4\pi \rho_w^{1/2} k} \frac{\tau^{1/2}}{r_{\text{eff}}^{5/2}}, \tag{B1}$$

TABLE A2. $\overline{\kappa}$ (time-averaged κ) calculated according to Eq. (2) with AMS-measured $\overline{m_i}$ as input listed in Table A1. κ_i is adopted from Table 1 of Petters and Kreidenweis (2007) for both the inorganic components and the organic one. The mass of NH_4^+ is divided to $(NH_4)_2SO_4$ and NH_4NO_3 by its molecular proportion assuming both sulfate and nitrate are fully neutralized as $(NH_4)_2SO_4$ and NH_4NO_3. Taking the upper limit of the κ value for the organic aerosols as $\kappa_{\text{org}} = 0.229$ during the BCB1 sampling for the 28 Feb case, we get $\overline{\kappa} = 0.392$.

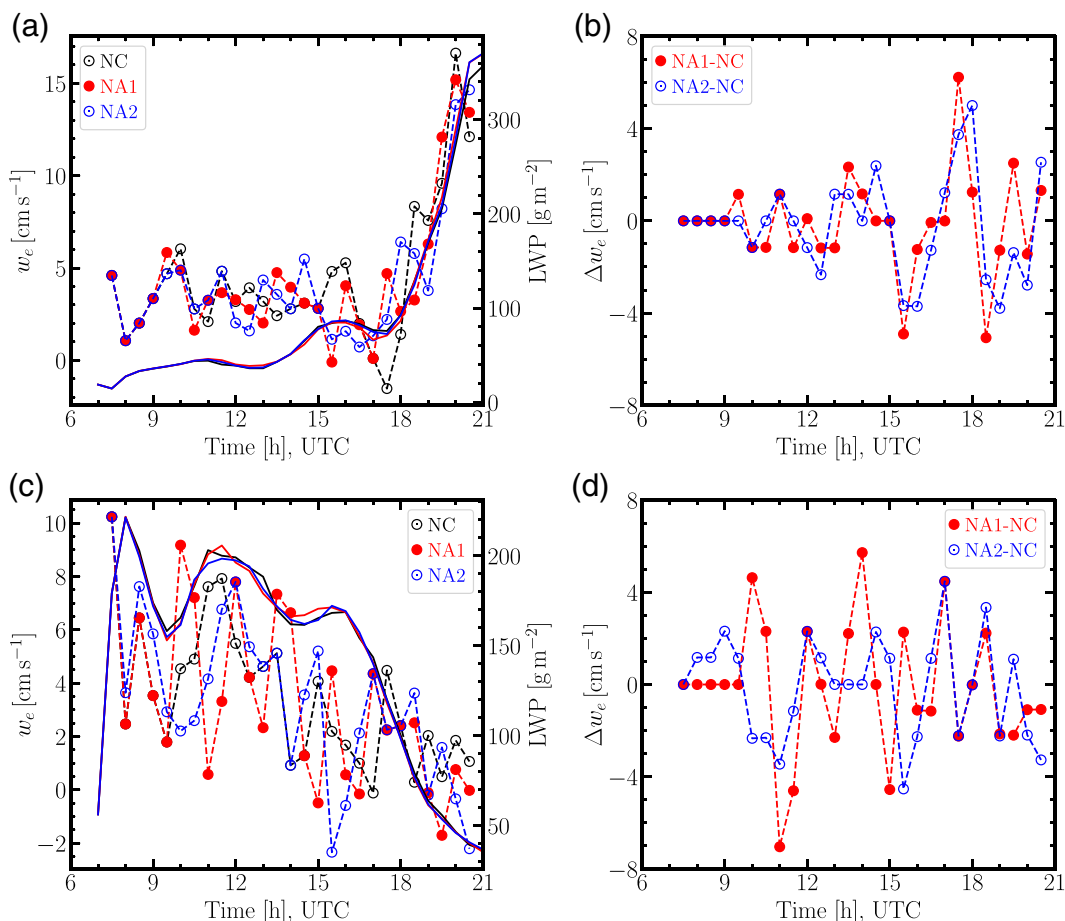| Component	Organic	$(NH_4)_2SO_4$	$(NH_4)NO_3$	$\overline{\kappa}$
$\rho_i(\text{g cm}^{-3})$		1.35	1.77	1.72
κ_i		0.1	0.61	0.67
0228				
BCB1	54.5%	30.0%	14.1%	0.313
BCB2	48.6%	35.1%	15.5%	0.341
0301				
BCB1	27.6%	60.8%	10.5%	0.451
BCB2	24.9%	43.5%	30.7%	0.479

FIG. C1. Entrainment rate $w_e = dz_i/dt - \langle w \rangle_{z_i}$ and the corresponding difference between NA and NC simulations Δw_e (circles) for the (a),(b) 28 Feb and (c),(d) 1 Mar cases, where the cloud-top height z_i is determined by the threshold $q_c \geq 0.02$ g kg^{-1}. $\langle w \rangle_{z_i}$ is the ERA5 large-scale vertical velocity at z_i. Solid lines in (a) and (c) represent the corresponding LWP.

where Γ (g m^{-4}) is the lapse rate due to condensation of water vapor and is estimated from the cloud-top temperature and pressure retrievals of *GOES-16*; $\rho_w = 1000$ kg m^{-3} is the density of water; $k = r_v^3/r_{\text{eff}}^3 = 0.8$ is assumed to be a constant with r_v the volume mean radius; and N_c is assumed to be height independent in Eq. (B1).

APPENDIX C

Entrainment Rate

Figure C1 shows the entrainment rate w_e.

REFERENCES

Ackerman, A. S., M. P. Kirkpatrick, D. E. Stevens, and O. B. Toon, 2004: The impact of humidity above stratiform clouds on indirect aerosol climate forcing. *Nature*, **432**, 1014–1017, https://doi.org/10.1038/nature03174.

——, and Coauthors, 2009: Large-eddy simulations of a drizzling, stratocumulus-topped marine boundary layer. *Mon.*

Wea. Rev., **137**, 1083–1110, https://doi.org/10.1175/2008 MWR2582.1.

Albrecht, B. A., 1989: Aerosols, cloud microphysics, and fractional cloudiness. *Science*, **245**, 1227–1230, https://doi.org/10.1126/science.245.4923.1227.

Aldhaif, A. M., D. H. Lopez, H. Dadashazar, and A. Sorooshian, 2020: Sources, frequency, and chemical nature of dust events impacting the United States East Coast. *Atmos. Environ.*, **231**, 117456, https://doi.org/10.1016/j.atmosenv.2020.117456.

——, ——, ——, D. Painemal, A. J. Peters, and A. Sorooshian, 2021: An aerosol climatology and implications for clouds at a remote marine site: Case study over Bermuda. *J. Geophys. Res. Atmos.*, **126**, e2020JD034038, https://doi.org/10.1029/2020JD034038.

Andrejczuk, M., W. W. Grabowski, J. Reisner, and A. Gadian, 2010: Cloud-aerosol interactions for boundary layer stratocumulus in the Lagrangian cloud model. *J. Geophys. Res.*, **115**, D22214, https://doi.org/10.1029/2010JD014248.

Bansmer, S. E., and Coauthors, 2018: Design, construction and commissioning of the Braunschweig Icing Wind Tunnel. *Atmos. Meas. Tech.*, **11**, 3221–3249, https://doi.org/10.5194/amt-11-3221-2018.

Baumgardner, D., and Coauthors, 2017: Cloud ice properties: In situ measurement challenges. *Ice Formation and Evolution in Clouds and Precipitation: Measurement and Modeling Challenges*, Meteor. Monogr., No. 58, Amer. Meteor. Soc., https://doi.org/10.1175/AMSMONOGRAPHS-D-16-0011.1.

Bellouin, N., and Coauthors, 2020: Bounding global aerosol radiative forcing of climate change. *Rev. Geophys.*, **58**, e2019RG000660, https://doi.org/10.1029/2019RG000660.

Bryan, G. H., J. C. Wyngaard, and J. M. Fritsch, 2003: Resolution requirements for the simulation of deep moist convection. *Mon. Wea. Rev.*, **131**, 2394–2416, https://doi.org/10.1175/1520-0493(2003)131<2394:RRFTSO>2.0.CO;2.

Chen, Y.-C., L. Xue, Z. J. Lebo, H. Wang, R. M. Rasmussen, and J. H. Seinfeld, 2011: A comprehensive numerical study of aerosol-cloud-precipitation interactions in marine stratocumulus. *Atmos. Chem. Phys.*, **11**, 9749–9769, https://doi.org/10.5194/acp-11-9749-2011.

Corral, A. F., and Coauthors, 2021: An overview of atmospheric features over the western North Atlantic Ocean and North American east coast—Part 1: Analysis of aerosols, gases, and wet deposition chemistry. *J. Geophys. Res. Atmos.*, **126**, e2020JD032592, https://doi.org/10.1029/2020JD032592.

Dagan, G., P. Stier, G. Spill, R. Herbert, M. Heikenfeld, S. C. van den Heever, and P. J. Marinescu, 2022: Boundary conditions representation can determine simulated aerosol effects on convective cloud fields. *Commun. Earth Environ.*, **3**, 71, https://doi.org/10.1038/s43247-022-00399-5.

DeCarlo, P. F., and Coauthors, 2008: Fast airborne aerosol size and chemistry measurements above Mexico City and central Mexico during the MILAGRO campaign. *Atmos. Chem. Phys.*, **8**, 4027–4048, https://doi.org/10.5194/acp-8-4027-2008.

de Roode, S. R., and Coauthors, 2019: Turbulent transport in the gray zone: A large eddy model intercomparison study of the CONSTRAIN cold air outbreak case. *J. Adv. Model. Earth Syst.*, **11**, 597–623, https://doi.org/10.1029/2018MS001443.

Endo, S., and Coauthors, 2015: RACORO continental boundary layer cloud investigations: 2. Large-eddy simulations of cumulus clouds and evaluation with in situ and ground-based observations. *J. Geophys. Res. Atmos.*, **120**, 5993–6014, https://doi.org/10.1002/2014JD022525.

Feingold, G., I. Koren, H. Wang, H. Xue, and W. A. Brewer, 2010: Precipitation-generated oscillations in open cellular cloud fields. *Nature*, **466**, 849–852, https://doi.org/10.1038/nature09314.

Fletcher, J., S. Mason, and C. Jakob, 2016: The climatology, meteorology, and boundary layer structure of marine cold air outbreaks in both hemispheres. *J. Climate*, **29**, 1999–2014, https://doi.org/10.1175/JCLI-D-15-0268.1.

Fridlind, A. M., and Coauthors, 2017: Derivation of aerosol profiles for MC3E convection studies and use in simulations of the 20 May squall line case. *Atmos. Chem. Phys.*, **17**, 5947–5972, https://doi.org/10.5194/acp-17-5947-2017.

Gelaro, R., and Coauthors, 2017: The Modern-Era Retrospective Analysis for Research and Applications, version 2 (MERRA-2). *J. Climate*, **30**, 5419–5454, https://doi.org/10.1175/JCLI-D-16-0758.1.

Ghan, S., and Coauthors, 2016: Challenges in constraining anthropogenic aerosol effects on cloud radiative forcing using present-day spatiotemporal variability. *Proc. Natl. Acad. Sci. USA*, **113**, 5804–5811, https://doi.org/10.1073/pnas.1514036113.

Glassmeier, F., F. Hoffmann, J. S. Johnson, T. Yamaguchi, K. S. Carslaw, and G. Feingold, 2021: Aerosol-cloud-climate cooling overestimated by ship-track data. *Science*, **371**, 485–489, https://doi.org/10.1126/science.abd3980.

Hersbach, H., and Coauthors, 2020: The ERA5 global reanalysis. *Quart. J. Roy. Meteor. Soc.*, **146**, 1999–2049, https://doi.org/10.1002/qj.3803.

Hu, Y., Z. J. Lebo, B. Geerts, Y. Wang, and Y. Hu, 2023: Vertical structure and ice production processes of shallow convective post-frontal clouds over the Southern Ocean in MARCUS. Part II: Modeling study. *J. Atmos. Sci.*, https://doi.org/10.1175/JAS-D-21-0272.1, in press.

Knop, I., S. E. Bansmer, V. Hahn, and C. Voigt, 2021: Comparison of different droplet measurement techniques in the Braunschweig Icing Wind Tunnel. *Atmos. Meas. Tech.*, **14**, 1761–1781, https://doi.org/10.5194/amt-14-1761-2021.

Lai, H.-W., F. Zhang, E. E. Clothiaux, D. R. Stauffer, B. J. Gaudet, J. Verlinde, and D. Chen, 2020: Modeling Arctic boundary layer cloud streets at grey-zone resolutions. *Adv. Atmos. Sci.*, **37**, 42–56, https://doi.org/10.1007/s00376-019-9105-y.

Lawson, R. P., D. O'Connor, P. Zmarzly, K. Weaver, B. Baker, Q. Mo, and H. Jonsson, 2006: The 2D-S (stereo) probe: Design and preliminary tests of a new airborne, high-speed, high-resolution particle imaging probe. *J. Atmos. Oceanic Technol.*, **23**, 1462–1477, https://doi.org/10.1175/JTECH1927.1.

Lee, S. S., J. E. Penner, and S. M. Saleeby, 2009: Aerosol effects on liquid-water path of thin stratocumulus clouds. *J. Geophys. Res.*, **114**, D07204, https://doi.org/10.1029/2008JD010513.

Li, X.-Y., and Coauthors, 2022: Large-eddy simulations of marine boundary layer clouds associated with cold-air outbreaks during the ACTIVATE campaign. Part I: Case setup and sensitivities to large-scale forcings. *J. Atmos. Sci.*, **79**, 73–100, https://doi.org/10.1175/JAS-D-21-0123.1.

McCoy, D. T., P. Field, H. Gordon, G. S. Elsaesser, and D. P. Grosvenor, 2020: Untangling causality in midlatitude aerosol–cloud adjustments. *Atmos. Chem. Phys.*, **20**, 4085–4103, https://doi.org/10.5194/acp-20-4085-2020.

Minnis, P., and Coauthors, 2008: Near-real time cloud retrievals from operational and research meteorological satellites. *Proc. SPIE*, **7107**, 710703, https://doi.org/10.1117/12.800344.

——, and Coauthors, 2021: CERES MODIS cloud product retrievals for Edition 4—Part I: Algorithm changes. *IEEE Trans. Geosci. Remote Sens.*, **51**, 2744–2780, https://doi.org/10.1109/TGRS.2020.3008866.

Moore, R. H., and Coauthors, 2021: Sizing response of the Ultra-High Sensitivity Aerosol Spectrometer (UHSAS) and Laser Aerosol Spectrometer (LAS) to changes in submicron aerosol composition and refractive index. *Atmos. Meas. Tech.*, **14**, 4517–4542, https://doi.org/10.5194/amt-14-4517-2021.

Noble, S. R., and J. G. Hudson, 2015: MODIS comparisons with northeastern Pacific in situ stratocumulus microphysics. *J. Geophys. Res. Atmos.*, **120**, 8332–8344, https://doi.org/10.1002/2014JD022785.

Painemal, D., and P. Zuidema, 2011: Assessment of MODIS cloud effective radius and optical thickness retrievals over the Southeast Pacific with VOCALS-REx in situ measurements. *J. Geophys. Res.*, **116**, D24206, https://doi.org/10.1029/2011JD016155.

——, P. Minnis, J. K. Ayers, and L. O'Neill, 2012: GOES-10 microphysical retrievals in marine warm clouds: Multi-instrument validation and daytime cycle over the southeast Pacific. *J. Geophys. Res.*, **117**, D19212, https://doi.org/10.1029/2012JD017822.

——, and Coauthors, 2021a: Evaluation of satellite retrievals of liquid clouds from the GOES-13 imager and MODIS over

the midlatitude North Atlantic during NAAMES campaign. *Atmos. Meas. Tech.*, **14**, 6633–6646, https://doi.org/10.5194/amt-14-6633-2021.

——, and Coauthors, 2021b: An overview of atmospheric features over the western North Atlantic Ocean and North American east coast—Part 2: Circulation, boundary layer, and clouds. *J. Geophys. Res. Atmos.*, **126**, e2020JD033423, https://doi.org/10.1029/2020JD033423.

Petters, M. D., and S. M. Kreidenweis, 2007: A single parameter representation of hygroscopic growth and cloud condensation nucleus activity. *Atmos. Chem. Phys.*, **7**, 1961–1971, https://doi.org/10.5194/acp-7-1961-2007.

Rosenfeld, D., Y. J. Kaufman, and I. Koren, 2006: Switching cloud cover and dynamical regimes from open to closed Benard cells in response to the suppression of precipitation by aerosols. *Atmos. Chem. Phys.*, **6**, 2503–2511, https://doi.org/10.5194/acp-6-2503-2006.

Sandu, I., J.-L. Brenguier, O. Geoffroy, O. Thouron, and V. Masson, 2008: Aerosol impacts on the diurnal cycle of marine stratocumulus. *J. Atmos. Sci.*, **65**, 2705–2718, https://doi.org/10.1175/2008JAS2451.1.

Seethala, C., and Coauthors, 2021: On assessing ERA5 and MERRA2 representations of cold-air outbreaks across the Gulf Stream. *Geophys. Res. Lett.*, **48**, e2021GL094364, https://doi.org/10.1029/2021GL094364.

Seifert, A., and K. D. Beheng, 2006: A two-moment cloud microphysics parameterization for mixed-phase clouds. Part 1: Model description. *Meteor. Atmos. Phys.*, **92**, 45–66, https://doi.org/10.1007/s00703-005-0112-4.

——, T. Heus, R. Pincus, and B. Stevens, 2015: Large-eddy simulation of the transient and near-equilibrium behavior of precipitating shallow convection. *J. Adv. Model. Earth Syst.*, **7**, 1918–1937, https://doi.org/10.1002/2015MS000489.

Seinfeld, J. H., and Coauthors, 2016: Improving our fundamental understanding of the role of aerosol–cloud interactions in the climate system. *Proc. Natl. Acad. Sci. USA*, **113**, 5781–5790, https://doi.org/10.1073/pnas.1514043113.

Sorooshian, A., and Coauthors, 2019: Aerosol–cloud–meteorology interaction airborne field investigations: Using lessons learned from the U.S. West Coast in the design of ACTIVATE off the U.S. East Coast. *Bull. Amer. Meteor. Soc.*, **100**, 1511–1528, https://doi.org/10.1175/BAMS-D-18-0100.1.

——, and Coauthors, 2020: Atmospheric research over the western North Atlantic Ocean region and North American east coast: A review of past work and challenges ahead. *J. Geophys. Res. Atmos.*, **125**, e2019JD031626, https://doi.org/10.1029/2019JD031626.

Stevens, B., and G. Feingold, 2009: Untangling aerosol effects on clouds and precipitation in a buffered system. *Nature*, **461**, 607–613, https://doi.org/10.1038/nature08281.

Tornow, F., A. S. Ackerman, and A. M. Fridlind, 2021: Preconditioning of overcast-to-broken cloud transitions by riming in marine cold air outbreaks. *Atmos. Chem. Phys.*, **21**, 12 049–12 067, https://doi.org/10.5194/acp-21-12049-2021

——, and Coauthors, 2022: Dilution of boundary layer cloud condensation nucleus concentrations by free tropospheric entrainment during marine cold air outbreaks. *Geophys. Res. Lett.*, **49**, e2022GL098444, https://doi.org/10.1029/2022GL098444.

Trepte, Q. Z., and Coauthors, 2019: Global cloud detection for CERES Edition 4 using Terra and Aqua MODIS data. *IEEE Trans. Geosci. Remote Sens.*, **57**, 9410–9449, https://doi.org/10.1109/TGRS.2019.2926620.

Twomey, S., 1977: The influence of pollution on the shortwave albedo of clouds. *J. Atmos. Sci.*, **34**, 1149–1152, https://doi.org/10.1175/1520-0469(1977)034<1149:TIOPOT>2.0.CO;2.

Voigt, C., and Coauthors, 2010: In-situ observations of young contrails—Overview and selected results from the CONCERT campaign. *Atmos. Chem. Phys.*, **10**, 9039–9056, https://doi.org/10.5194/acp-10-9039-2010.

Wang, H., and G. Feingold, 2009a: Modeling mesoscale cellular structures and drizzle in marine stratocumulus. Part I: Impact of drizzle on the formation and evolution of open cells. *J. Atmos. Sci.*, **66**, 3237–3256, https://doi.org/10.1175/2009JAS3022.1.

——, and ——, 2009b: Modeling mesoscale cellular structures and drizzle in marine stratocumulus. Part II: The microphysics and dynamics of the boundary region between open and closed cells. *J. Atmos. Sci.*, **66**, 3257–3275, https://doi.org/10.1175/2009JAS3120.1.

Zhang, Z., X. Dong, B. Xi, H. Song, P.-L. Ma, S. J. Ghan, S. Platnick, and P. Minnis, 2017: Intercomparisons of marine boundary layer cloud properties from the ARM CAP-MBL campaign and two MODIS cloud products. *J. Geophys. Res. Atmos.*, **122**, 2351–2365, https://doi.org/10.1002/2016JD025763.